MASTER THESIS
TECHNICAL MEDICINE

MEDICAL IMAGING & INTERVENTIONS

FDG-DOSE PREDICTION AND SMALL LESION DETECTION USING ADVANCED PET TECHNOLOGY

T J GERRITSE

12-02-2019

TITLE PAGE

T.J. Gerritse

Defense:	February 12th 2019, 1:30 PM at Carré 3022, University of Twente, Enschede
Master track:	Technical Medicine, Imaging and Intervention, University of Twente
Location:	Isala Hospital, Zwolle
Title:	FDG-dose prediction and small lesion detection using advanced PET technology

Graduation committee

Chairman & Technical supervisor at UT:	Prof.dr.ir. C.H. Slump
Medical supervisor at Isala:	Prof.dr. P.L. Jager
Technical supervisor at Isala:	Dr. J.A. van Dalen
Process supervisor:	Drs. R.J. Haarman
Daily supervisor & extra member:	D. Koopman, MSc
Extern member:	Prof.dr. L. de Geus-Oei

Preface

Beste lezer,

Voor u ligt de scriptie ‘FDG-dose prediction and small lesion detection using advanced PET technology’. Deze scriptie is geschreven in het kader van mijn afstuderen van de opleiding Technical Medicine van Universiteit Twente. Het betreft de master track Medical Imaging & Interventions. Het onderzoek heeft plaatsgevonden vanuit de afdeling Nucleaire Geneeskunde van Isala Zwolle. Het afstudeertraject is begonnen in maart 2018 en afgerond in januari 2019 met een verdediging in februari 2019.

Mede dankzij de intensieve begeleiding van mijn dagelijkse stagebegeleiders vanuit Isala: Daniëlle Koopman, Jorn van Dalen en Piet Jager en begeleiding vanuit Universiteit Twente door Kees Slump, heb ik mijn afstudeertraject tot een goed einde kunnen brengen. Hiervoor ben ik hen dankbaar, want het is daardoor een zeer leerzaam jaar geweest. De ontwikkeling die ik dit jaar doorgemaakt heb als persoon en als Technisch Geneeskundige is mede tot stand gekomen door procesbegeleiding van Rian Haarman en intervisiebijeenkomsten met Bernice Wulterkens en Tom Berfelo. Ik wil hen bedanken voor de procesbegeleiding en inzicht gevende gesprekken gedurende mijn derde en vierde M2 stages en mijn M3 stage. Overigens kan ik hierbij de gesprekken met studiegenoten, begeleiders en collega’s niet onbesproken laten, want ook op die momenten heb ik veel inzicht verkregen in mijn eigen kwaliteiten, mijn voorkomen en mijn interesses. Daarnaast heb ik mijn onderzoek compleet kunnen maken met de data van 2 nieuwe PET systemen, wat niet mogelijk was geweest zonder de bereidheid en hulp van Ralph Berendsen (Zuyderland Medisch Centrum) en Joyce van Sluis (Universitair Medisch Centrum Groningen). Tot slot wil ik Lioe-Fee de Geus bedanken als buitenlid van de afstudeercommissie.

Ik hoop dat u met veel plezier mijn scriptie zult lezen.

Tessa Gerritse

Zwolle, 18 januari 2019

Summary

Cancer is one of the most common diseases of our time. More than 350,000 people live with cancer and its consequences in the Netherlands, and since 7 years more than 100,000 people are diagnosed with cancer every year. Early detection and accurate diagnosis are essential and positron emission tomography (PET) using ^{18}F-fluordesoxyglucose (^{18}F-FDG) is frequently used for these purposes. The most recent development in PET technology is the use of digital detectors, potentially improving the sensitivity, spatial resolution and temporal resolution as compared to conventional PET systems. These improvements offer the possibility to shorten the scan duration or to use less FDG activity. Another possibility is to improve the image quality of PET scans, enabling improved small lesion detection. The aims were 1) to develop a model that predicts the required FDG activity and scan time per bed position for a standardized image quality based on the NEMA specifications of a given PET/CT system and 2) to evaluate the potential value of ultra-high-resolution (uHR) reconstructions in digital PET imaging to improve small lesion detection, compared to high-resolution (HR) reconstructions.

For the development of a prediction model for the required FDG activity and scan time per bed position for a standardized image quality, we included 6 state-of-the-art EARL accredited PET/CT systems and performed a phantom study. Within this study we compared the 6 PET systems with each other in terms of required FDG activity and scan duration when image quality was standardized according to EARL accreditation specifications. By means of this comparison a so-called System Constant was determined per PET system. Furthermore, the effective sensitivity of each of the PET systems was determined, based on their NEMA specifications. Based on a strong correlation between the System Constant and the effective sensitivity of a given PET system a prediction model was derived. Large differences between PET systems, which currently dominate the market, imply large differences in the System Constant, which directly influences clinical routine and costs per patient. In the future, the prediction model is therefore an important tool to use for the comparison between multiple PET systems when purchasing a new PET system.

For the evaluation of the potential value of uHR reconstructions in digital PET imaging compared to HR reconstructions, we included 31 patients for a patient study. PET data was reconstructed with both HR and uHR reconstruction settings and assessed visually by three nuclear medicine physicians, based on contrast, noise, and diagnostic certainty. Within the group of included patients, 112 lesions were included for a quantitative analysis to compare measurements of lesion parameters between both reconstructed images. A small quantitative increase has been found in the SUVs and lesion-to-background ratio in the uHR reconstruction as compared to the HR reconstruction. In addition, the measured lesion volume decreases significantly. We can therefore conclude that the uHR reconstruction ensures that the small lesion detection is less hampered by the partial-volume effect. However, we do not expect these changes to be relevant for the purpose of FDG-PET in current clinical practice, which is also reflected in the visual assessment, where nuclear medicine physicians had no clear preference for the uHR reconstruction. Should the value of exact measurements of lesion parameters increase in the future, then the uHR reconstruction would be useful, but otherwise the potential value of uHR reconstructions in digital PET imaging for the improved detection of small lesions is minimal.

Abbreviations

COV	Coefficient Of Variation
cPET	conventional Positron Emission Tomography
CT	Computed Tomography
dPET	digital Positron Emission Tomography
EANM	European Association of Nuclear Medicine
EARL	EANM Research Ltd.
FDG	Fluordesoxyglucose
FOV	Field Of View
HR	High Resolution
IQ	Image Quality
LB_{ratio}	Lesion-to-Background ratio
NEC	Noise Equivalent Count
NEMA	National Electrical Manufacturers Association
PET	Positron Emission Tomography
PMT	Photomultiplier Tube
PSF	Point-Spread-Function
PVE	Partial-Volume Effect
QC	Quality Control
RC	Recovery coefficient
RC_{max}	Maximum activity concentration Recovery Coefficient
RC_{mean}	Mean activity concentration Recovery Coefficient
ROI	Region Of Interest
SiPM	Silicon Photomultiplier Tube
SNR	Signal-to-Noise Ratio
SUV_{max}	Maximum standardized uptake value
SUV_{mean}	Mean standardized uptake value
TOF	Time-Of-Flight
uHR	ultra-High Resolution
VOI	Volume Of Interest
VOI-MAX	The VOI that results in the RC_{max}
VOI-A50	The VOI that results in the RC_{mean}

Thesis outline

This thesis is divided into two topics. Both are related to developments in the field of PET imaging and in particular to digital PET technology.

Chapter 1 contains a general introduction and a description of two main goals followed by a background section. In this background section relevant information about PET technology, the EARL accreditation program, patient specific FDG activity, and the PETPET study is described.

The first aim was to develop a model that predicts the required FDG activity and scan time per bed position for a desired image quality based on the NEMA specifications of any given PET/CT system. In Chapter 2 of this thesis a method is explained on how to develop such a model. Furthermore, this method has been executed by means of 6 different PET/CT systems, of which the results are also discussed in Chapter 2.

The second aim was to investigate the potential value of ultra-high-resolution (uHR) reconstructions in digital PET imaging to improve small lesion detection, compared to high-resolution (HR) reconstructions. Chapter 3 describes the patient study we performed in which uHR reconstructed images were compared both visually and quantitatively with HR reconstructed images. The value of uHR reconstructions was evaluated based on the results of this study.

Table of contents

TITLE PAGE	III
PREFACE	V
SUMMARY	VII
ABBREVIATIONS	IX
THESIS OUTLINE	XI
CHAPTER I	1
CHAPTER II	11
CHAPTER III	23
REFERENCES	37

CHAPTER I

Introduction

Cancer is one of the most common diseases of our time. More than 350,000 people live with cancer and its consequences in the Netherlands, and since 7 years more than 100,000 people are diagnosed with cancer every year (1). Positron emission tomography (PET) using ^{18}F-fluordesoxyglucose (^{18}F-FDG) is frequently used for diagnosing, staging, restaging and therapy response assessment of tumors (2). FDG-PET has been proven to be a sensitive imaging modality for these purposes (3–7).

In recent years, progress has been made in several areas in the field of PET/Computed Tomography (CT) such as improvements in detector design and architecture as well as the implementation of time-of-flight (TOF) technology. This significantly improved the PET image quality and created possibilities of reducing radiotracer dose and scanning time (8–10). The most recent development is the use of digital detectors. This new digital PET (dPET) is based on a digital technique for photon detection. The classic photomultiplier tube (PMT) has been replaced by a chip in which each pixel element is directly coupled to a scintillation crystal (11). This integration enables true digital photon counting without the need for a digital conversion. A digital detector potentially improves the sensitivity, spatial resolution and temporal resolution as compared to conventional PET (cPET) systems (11,12). Hence, with a digital detector, the image quality of PET scans can be improved; allowing smaller lesions to be detected better, but it also offers possibilities to shorten the scan duration or to use a lower dose of administered tracer activity.

Important characteristics of a PET/CT system that may be decisive for the image quality are; the sensitivity of the detectors, the time-of-flight (TOF) performance, and the spatial resolution. These characteristics differ between PET systems (13). In addition, the properties of a system as specified by National Electrical Manufacturers Association (NEMA) are based on ideal conditions that do not correspond to clinical practice. For these reasons it is complicated to predict how various PET/CT systems relate to one another in terms of image quality, required administered radioactivity and scan duration prior to having any practical experience. While the scan duration has its effect on clinical practice, the required amount of radioactivity per patient directly affects costs and radiation exposure.

Therefore, the first aim of this thesis was to develop a model that relates important characteristics of a given PET/CT system to minimal image quality requirements and minimally required administered radioactivity and scan duration.

Furthermore, within a single PET/CT system several reconstruction settings are available. Chosen settings have a large effect on the image quality of a PET scan. In order to take advantage of the better spatial and temporal resolution of new digital PET/CT systems, so that smaller lesions can be detected better or earlier, manufacturers provided new possibilities in reconstruction settings. In general, better small lesion detection is enabled by

using smaller voxels, introducing point-spread-function (PSF) modeling or by using less post-filtering in the image reconstruction (13).

As one of the first five in the world, the Isala Department of Nuclear Medicine has a dPET system since October 2017 (Vereos), which was developed by Philips Healthcare. This system provides the possibility to use 1x1x1 mm^3 voxel (ultra-high resolution) reconstructions in addition to 2x2x2 mm^3 (high resolution) and 4x4x4 mm^3 voxel reconstructions. For these 1x1x1 mm^3 voxel reconstructions, a phantom study has shown that this ultra-high resolution (uHR) reconstruction has the potential to improve the detection of small lesions (14,15). However, the impact on patient data has not yet been investigated and it is unknown how nuclear medicine physicians evaluate these uHR PET images in clinical practice.

Therefore, the second aim of this thesis was to investigate the potential value of uHR reconstructions in digital PET imaging to improve small lesions detection quantitatively and visually, compared to HR reconstructions, in patients with cancer.

Background

FDG-PET/CT

PET is a technique that computes the three-dimensional distribution of a radioactive tracer, which allows non-invasive assessment of physiological and malignant tissue. CT is a widespread form of medical diagnosis in which the anatomy of the human body can be accurately imaged in three dimensions. The combination of both modalities in a single device offers the possibility to relate physiological information, such as malignant tissue, to the anatomical location. In addition, the CT is used for photon attenuation-correction of the PET images.

PET imaging is particularly valuable for oncological applications with the use of ^{18}F-FDG. ^{18}F is a cyclotron-produced radioisotope of fluorine that emits positrons and has a half-life of 109.7 minutes (2). FDG is a glucose analogue and its tissue-accumulation is proportional to the amount of glucose utilization. Increased glucose consumption is a characteristic of most tumor types (2,16,17).

After intravenous FDG administration, the patient typically has to wait 60 minutes while lying on a bed. In this way, the radiotracer has the time to accumulate in glucose-consuming tissues, without accumulating in muscle tissue. The radionuclide in the radiotracer decays and the resulting positrons subsequently collide with negatively charged electrons after travelling a short distance (typically 1 mm) within the body (18), which is demonstrated in Figure 1. This collision results in annihilation, producing two 511 keV photons in opposite directions. The detector ring, surrounding the patient, detects these photons simultaneously at 180 degrees to one another (2,18). Only photons that trigger the opposite detectors at nearly the same time will be accepted.

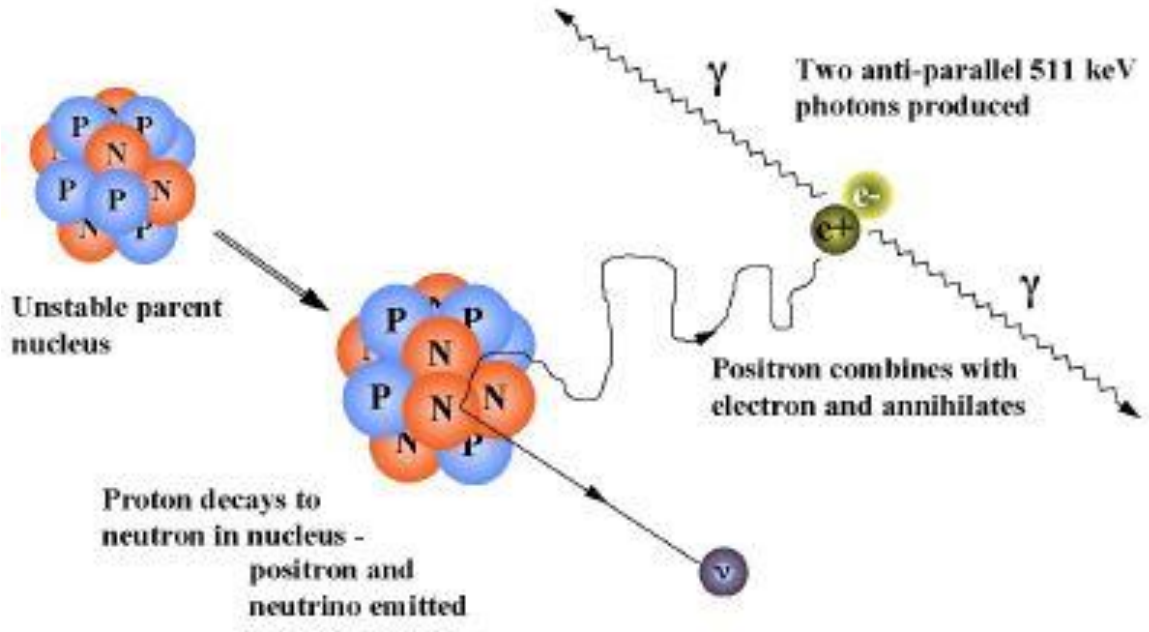

Figure 1: Positron emission and annihilation. Positrons are emitted by the unstable radioisotope and combine with an electron to annihilate into two 511 keV photons that depart in opposite direction (19).

Conventional vs. Digital

The main difference between conventional and digital PET/CT-systems is the way in which the photons are detected and converted into an electrical signal. The PMTs of the conventional systems are replaced by a digital silicon photomultipliers (SiPM) in the shape of a chip (11,12). This technology was developed because PMT design had reached its limits in counting performance due to the relatively large size of the device (Figure 2A) and the timing resolution (11).

In a conventional PET, the photons that resulted from annihilation convert into visible light by interaction with a scintillation crystal (19). This scintillation crystal is coupled to a PMT, which generates an electrical signal in response to the light (19). In the dPET of Philips Healthcare (Vereos), the visible photons produced by scintillation are counted directly by digital SiPMs, resulting in a pure binary signal (Figure 3) (11). This 1:1 coupling allows for a much higher count rate capability compared to analog systems (12). Figure 2B shows a comparison of photon detection using conventional PMTs and digital SiPMs with 1:1 detector coupling.

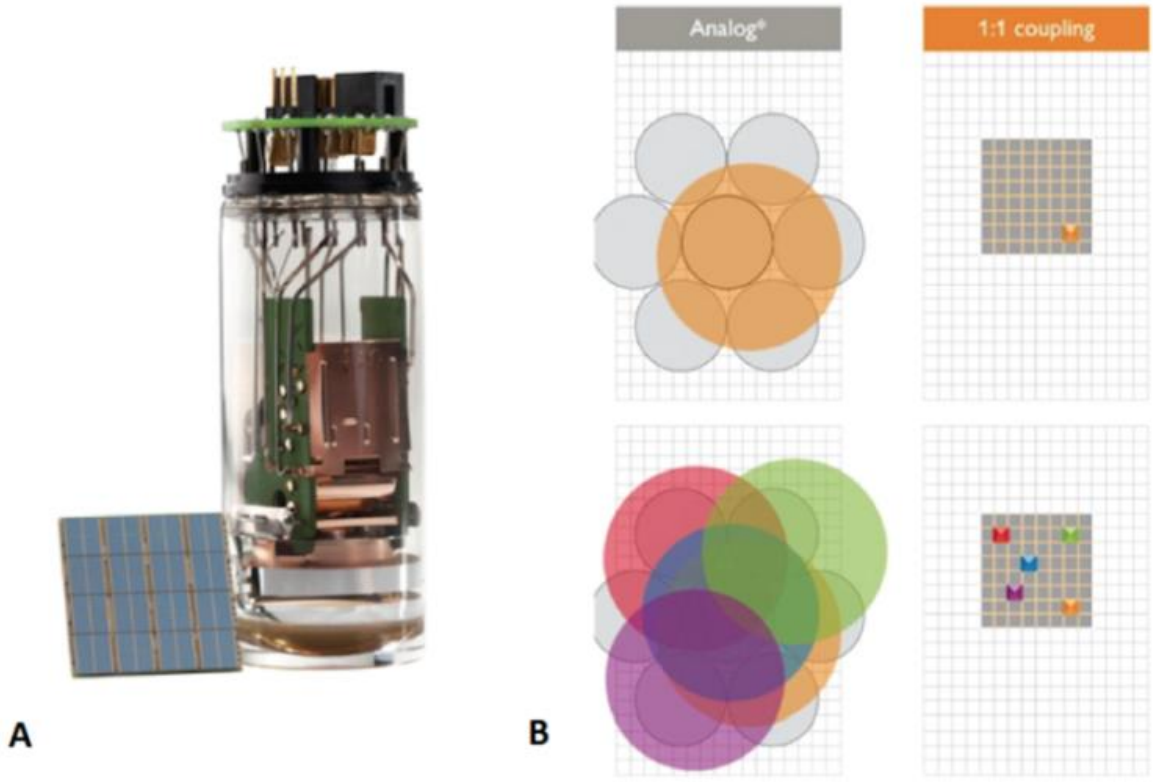

Figure 2: A. Comparison in size between the conventional PMT (right) and a SiPM with 1:1 detector coupling (left). **B.** Photon detection using conventional PMTs (left) and SiPMs in the Vereos dPET (right). The digital approach results in higher spatial and timing resolution (12).

The use of digital SiPMs increases the intrinsic timing resolution, which leads to improved sensitivity and spatial resolution. Furthermore, with the 1:1 coupling, the identification of scintillation photons is uniform across the entire detector, resulting in more accurate photon detection and the elimination of edge effects and decoding bias.

The EARL FDG-PET/CT accreditation program

Standardization and harmonization of FDG-PET imaging allows for comparison and exchange of FDG uptake measurements across patients, scanners and medical centers (2). For this purpose the European Association of Nuclear Medicine (EANM) has published general guidelines for FDG-PET imaging of tumors (2,20). In addition, an EANM research Ltd (EARL) has set up the EARL FDG-PET/CT accreditation program, which can help imaging sites to meet requirements as indicated by the guidelines (21). EARL provides FDG-PET accreditation for clinical trials in order to contribute to a minimum standard of PET/CT system performance. To attain and maintain PET/CT EARL accreditation, phantom measurements are required. Therefore, an image quality and recovery coefficient quality control procedure (IQRC QC) has been developed (2,20,21).

Part of the EARL accreditation procedure is the use of a NEMA NU2-2001 IQ Phantom, which contains six fillable spheres inside a background compartment. A schematic image of the phantom is shown in Figure 3. After filling the IQ phantom with a FDG-concentration, an activity concentration of about 20 kBq/mL is obtained in the spheres and an activity concentration of about 2 kBq/mL in the background compartment at the intended start-time of the phantom PET scan. This activity concentration in the background compartment represents a general uptake in a 75kg patient who received 300 MBq activity and is scanned at 1 hour post injection (21). The phantom is then positioned in such a way that the spheres are located at the center of the axial field of view and a routine “whole-body” FDG-PET scan is acquired with at least 10 minutes per bed position. After collection of the phantom data, the image reconstruction is performed conform specifications by EANM-guidelines. Finally, the reconstructed images are analyzed and compared to the EARL accreditation specifications.

Figure 3: This NEMA NU2-2001 IQ phantom has an interior length of 18 cm and contains 6 fillable spheres. From large to small, the spheres have an inner diameter of 37, 28, 22, 17, 13, and 10 mm. The large background compartment has a volume of 9.7 L

The maximum and mean recovery coefficients (RCs) of all six spheres are measured and compared to the ranges as specified by EARL. The maximum activity concentration recovery coefficient (RC_{max}) of a sphere is defined as the maximum pixel value within a sphere as measured on the reconstructed PET image, divided by the true FDG activity in the sphere at the time of acquisition (2). The mean activity concentration recovery coefficient (RC_{mean}) of a sphere is determined by creating a volume of interest (VOI) at 50% of the maximum pixel value, corrected for background uptake (2). To obtain RC_{mean}, the mean pixel value within this VOI is divided by the true FDG activity in the sphere at the time of acquisition (22). In Table 1 the current EARL accreditation specifications are summarized (23).

Table 1: Recovery coefficient (RC) specifications for VOI-MAX and VOI-A50 for all six spheres of the NEMA NU2-2001 IQ phantom (23).

		VOI-MAX		VOI-A50	
Sphere Diameter (mm)	Sphere Volume (mL)	Minimal RC	Maximal RC	Minimal RC	Maximal RC
37	26.52	0.76	0.89	0.95	1.16
28	11.49	0.72	0.85	0.91	1.13
22	5.57	0.63	0.78	0.83	1.09
17	2.57	0.57	0.73	0.73	1.01
13	1.15	0.44	0.60	0.59	0.85
10	0.52	0.27	0.43	0.34	0.57

Patient specific FDG activity

PET image quality is influenced by the patient's body weight (24,25). When a fixed FDG activity and scan duration is used, any body weight higher than average will result in more photon attenuation and higher scatter fractions (26,27). By increasing either FDG activity or scan duration this effect can be compensated (26,28). Therefore, the most recent guideline for FDG-PET imaging recommends prescribing FDG activity as a function of scan duration, type of scanner, reconstruction-settings, and a patient's body weight (20). A quadratic relation between FDG activity and the patient's body weight is recommended (29).

Koopman et al. published a step by step manual on how to obtain a formula, which describes the FDG activity to administer depending quadratically on the patient's body weight while satisfying EANM accreditation specifications (22). Figure 4 summarizes this manual in a flowchart. Up to and including Step 4, the protocol is identical to the IQRC QC procedure, which is briefly described in the previous section. In steps 5 through 7, reconstruction at shorter scan durations are used to determine the minimum required scan duration for standardized image quality. Based on these data, a formula is derived in step 8 that describes the relation between the patient's body weight and the required FDG activity and scan duration to ensure standardized image quality. A more extensive explanation of these steps is described in the methods section (subsection data analysis) of Chapter 2.

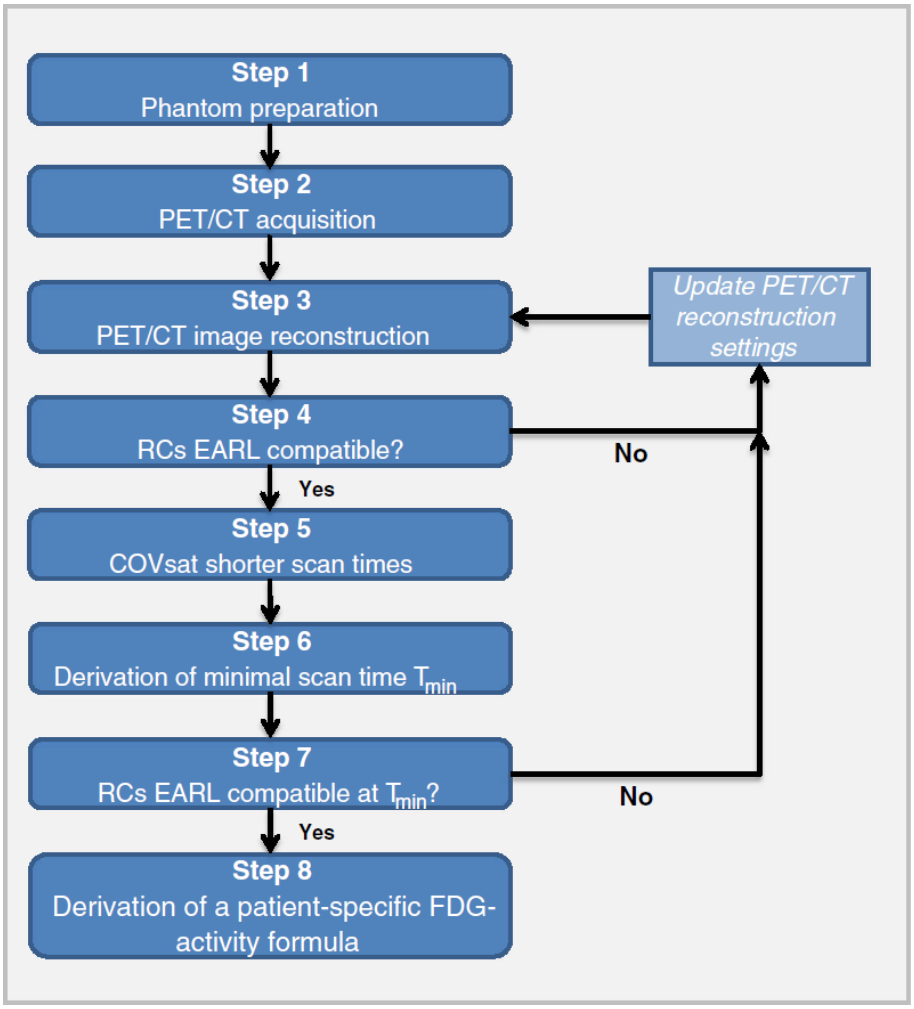

Figure 4: Flowchart demonstrating the step by step manual on how to define a patient-specific FDG activity formula (22).

The PETPET-study

The Isala department of nuclear medicine has a dPET system (Vereos) in addition to a cPET system (Ingenuity). Both PET/CT systems were developed by Philips Healthcare. In order to explore the areas in which this new dPET may offer improvement compared to the cPET, the Isala department of Nuclear Medicine has launched the so-called PETPET study. The primary objective of this study is to investigate how the diagnostic outcome of dPET compares to the outcome of cPET in patients referred for (re)staging of cancer. The secondary objective is to evaluate the image quality in both quantitative and qualitative terms of dPET as compared to cPET (30). This study was approved by the local medical ethics committee (Isala, Zwolle). Inclusion of patients and collection of data is still ongoing. Patients who participate in this study undergo two FDG-PET/CT scans in succession, one of which is on the cPET and the other on the dPET.

Patients are selected for the PETPET study if they are referred to the Isala department of nuclear medicine for a FDG-PET/CT with suspected or proven lung carcinoma, esophageal carcinoma, or breast cancer for either diagnosis, staging, or follow-up examination. Patients with any other kind of suspected or proven primary tumors (miscellaneous cancers) are only included when they are referred for primary diagnosis. Candidates for the study are excluded if they are either; younger than 18 years of age, incapacitated adults, pregnant, prisoner, or unable to undergo two PET/CT scans consecutively. Patients may participate in the PETPET study no more than once and can only participate if they have signed an informed consent form. (30)

The PET scan order is randomized per week (30). The study is designed in this way to prevent a possible bias due to the effect of the time between FDG administration and PET acquisition on FDG uptake measurements. From preparation to the first PET scan, the procedure is identical to the regular FDG-PET/CT procedure in our department with the only exception that the administered FDG activity is 20% higher for patients who participate in the PETPET study. A dedicated dose protocol, depending quadratically on patient's body weight, is implemented using the following formula:

$$A \cdot t_1 = 6.22 \cdot w^2$$

In this formula *A* is the FDG activity to administer in MBq, t_1 the time per bed position for the first scan in seconds (s), and *w* the body weight in kilograms (kg). The maximum FDG activity to be administered is set at 600 MBq, which is reached at a body weight of 118 kg. The minimal FDG activity to be administered is set at 216 MBq, which is reached at a body weight of 50 kg. The time per bed position for the first scan is 72 seconds per bed position for all patients ≤ 80 kg and 144 seconds per bed position for all patients > 80 kg. The resulting FDG activity to administer per body weight is shown in Figure 5. To cover the whole body region, on average 11 bed positions are required. This results in total PET acquisition times of approximately 13 and 26 minutes for patients with body weight ≤ 80 kg and > 80 kg respectively. Furthermore, attenuation CT acquisition takes around 5 minutes in all patients.

The first scan is started about 60 minutes after FDG administration and the second scan as soon as possible after the first scan, which is typically 80 to 110 minutes after FDG administration (30). In order to compensate for the decay of the tracer and to ensure comparability of the FDG uptake between the two scans, the scan duration of the second

scan is prolonged as compared to the scanning time of the first scan. This extension is calculated just before the second scan using the following formula:

$$t_2 = (0.5^{\frac{\Delta T}{T_{1/2}}})^{-1} \cdot t_1$$

In this formula t_2 is the time per bed position for the second scan in seconds (s), ΔT is the time between the start time of the first scan and the start time of the second scan in minutes (min), $T_{1/2}$ is the half-life of the tracer in minutes (min), and t_1 is the time per bed position for the first scan in seconds (s).

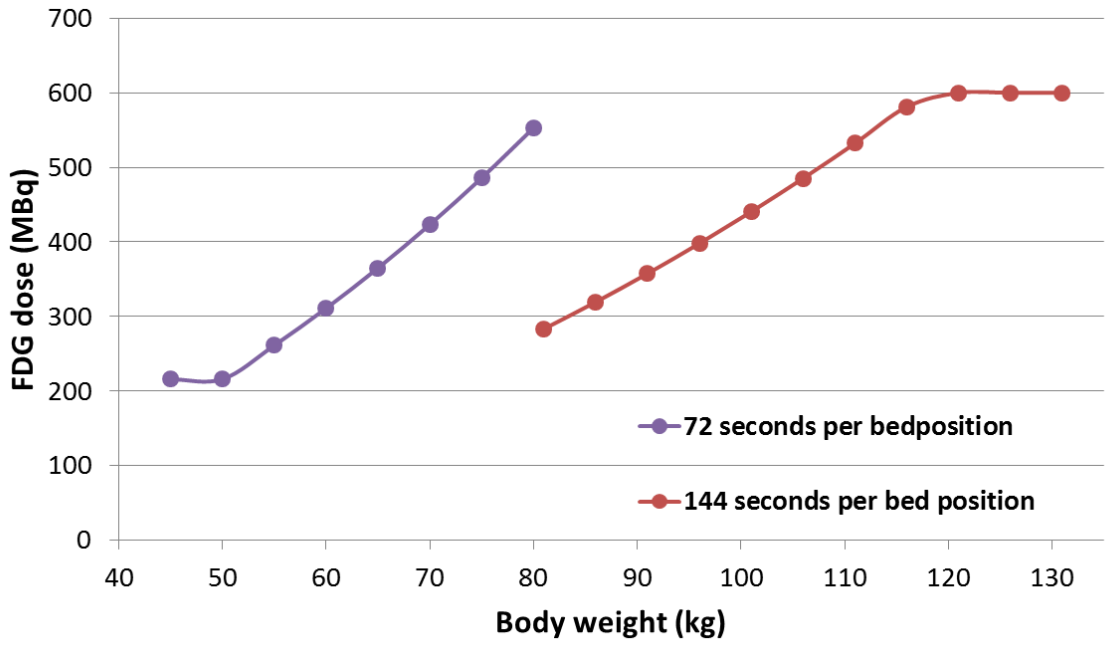

Figure 5: A dedicated dose protocol, depending quadratically on a patient's body weight, using the formula $A \cdot t = 6.22 \cdot w^2$.

CHAPTER II

Predicting FDG activity and scan duration to obtain standardized PET image quality

Abstract

BACKGROUND: In the last decade, progress has been made in several areas in the field of PET/CT and there is a large variation in technical specifications between PET systems. It is complicated to predict how any PET system will perform in clinical practice compared to other PET systems. Therefore, our aim was to develop a model that predicts the required FDG activity and scan time per bed position for a standardized image quality based on the NEMA specifications of a given PET/CT system.

METHOD: Six state-of-the-art PET/CT systems were included and a patient-specific FDG activity formula while complying to EARL accreditation specifications was determined for each system by means of a phantom study. From these formulas, the so-called "System Constant (C_{sys})" was derived per PET system and correlated to the effective sensitivity (S_e), which is based on NEMA specifications. From the power-law fit of this correlation, a predictive model was derived.

RESULTS: A power-law fit describing the relation between C_{sys} and S_e with $R^2 = 0.79$ and equation: $C_{sys} = 10.62 \cdot S_e^{-0.51}$ ($R^2 = 0.79$), resulted in a body-weight dependent model that predicts the required product of FDG activity and scan time, based on NEMA specifications of any given PET/CT system with: $A \cdot t = 10.62 \cdot S_e^{-0.51} \cdot w^2$.

CONCLUSION: A prediction model was developed, based on the strong correlation between System Constant and effective sensitivity of a PET system. Due to large difference between PET systems and their impact on clinical practice, the prediction model is an important tool to use for the comparison between multiple PET systems when purchasing a new PET system.

Introduction

PET using ^{18}F-FDG is frequently used for diagnosing, staging, restaging and therapy response assessment of tumors (2). FDG-PET has been proven to be a sensitive imaging modality for these purposes (3–7).

In the last decade, progress has been made in several areas in the field of PET/CT such as improvements in detector design and architecture as well as the implementation of TOF technology, which significantly improved image quality and created possibilities of reducing radiotracer dose and scanning time (8–10). The most recent development in PET technology is the use of digital detectors, potentially improving the sensitivity, spatial resolution and temporal resolution as compared to conventional PET systems. (11,12). These improvements are especially important when accurate FDG uptake measurements are necessary.

Important technical specifications of any PET system are crystal size, type of photon detector, system sensitivity, spatial resolution, TOF timing resolution, and type of PSF modeling (13). These specifications are different for every PET system. In addition, the properties of a system reflected in the NEMA specifications, are based on ideal conditions that do not directly correspond to clinical practice. For these reasons it is complicated to predict how any PET system will perform in clinical practice prior to having any practical experience with the system. For clinical practice, it is particularly useful to know how much administered activity and scan duration per patient is required to achieve a certain image quality, because it directly affects daily scheduling of scans, radiation exposure and FDG costs per patient. Therefore, in the process of purchasing a new PET system, it is helpful to know how the image quality of a given PET system relates to the required FDG activity and scan duration to achieve standardized image quality.

Our aim was to develop a model that predicts the required FDG activity and scan time per bed position for a standardized image quality based on the NEMA specifications of a PET/CT system.

Methods

In order to establish such a model, we compared 6 state-of-the-art EARL accredited PET/CT systems with each other in terms of image quality and minimally required FDG activity and scan duration. We performed a phantom study, using the NEMA NU2-2001 IQ phantom, which was prepared according to the IQRC QC procedure by EARL (21).

Data acquisition

The IQ phantom scans were acquired with 6 different PET/CT systems, which are described in Table 1. For all PET systems, the scan duration was at least 10 minutes and a list mode acquisition was used if possible. List mode enables reconstructions of shorter scan durations. If list mode was not an option, repeated acquisitions were performed at shorter scan durations.

Data Reconstruction

For each included PET system, the reconstruction settings were initially chosen such that the image quality fulfilled the EARL accreditation specifications. Settings have been adjusted in

such a way that the variance between the recovery coefficient (RC) curves of the 6 PET systems was as small as possible: for the Discovery MI (GE Healthcare) the matrix size was changed from 192x192 to 128x128 and for the Biograph mCT TrueV (Siemens) the Gaussian smoothing filter was increased from 7.0 to 7.5 mm. Appendix A.1 elaborates on how we tested several reconstruction settings. The final reconstruction settings are displayed in Table 2.

Table 1: Description of the 6 PET/CT systems that were compared to each other in terms of image quality and minimally required FDG activity and scan duration. Phantom data of the Biograph Vision were made available to us and consisted of just one scan with a scan duration of 10 minutes. Therefore, reconstructions at shorter scan duration were not available for this PET system.

Name	Manufacturer	Location	Shorter scan durations (s)
Ingenuity TF	Philips Healthcare	Isala, Zwolle	480. 360, 240, 120, 60, 30, 15, 8
Vereos	Philips Healthcare	Isala, Zwolle	480. 360, 240, 120, 60, 30, 15, 8
Discovery D690	GE Healthcare	Isala, Zwolle	480. 360, 240, 120, 60, 30, 15, 8
Discovery MI	GE Healthcare	Zuyderland, Heerlen	120, 60, 30
Biograph mCT TrueV	Siemens	Treant, Emmen	480. 360, 240, 120, 60, 30, 15, 8
Biograph Vision	Siemens	UMCG, Groningen	-

Table 2: PET data were reconstructed according to these settings per PET/CT system, to fulfil the EARL accreditation specifications.

Manufacturer	**Philips**		**GE**		**Siemens**	
PET/CT system	Ingenuity TF	Vereos	Discovery D690	Discovery MI	Biograph mCT TrueV	Biograph Vision
OSEM + TOF	**+**	**+**	**+**	**+**	**+**	**+**
PSF	**-**	**-**	**-**	**-**	**+**	**+**
Iterations	3	3	2	2	2	8
Subsets	43	15	24	34	21	5
Matrix	144 x 144	144 x 144	256 x 256	128 x 128	200 x 200	220 x 220
Voxels (mm3)	4 x 4 x 4	4 x 4 x 4	2.7 x 2.7 x 3.3	5.5 x 5.5 x 2.7	4.1 x 4.1 x 3	3.3 x 3.3 x 1.6
Smoothing filter	"normal"	Gaussian 3 mm	Gaussian 6.4 mm	Gaussian 7 mm	Gaussian 7.5 mm	Gaussian 7 mm

Data Analysis

Quantitative measurements were performed on a dedicated workstation (IntelliSpace Portal, Philips Healthcare). Based on the reconstructed images of all 6 PET systems, the RC_{max} of the spheres was calculated, using the following equation:

$$RC_{max} = \frac{PV_{max}}{A_{true}}$$

PV_{max} is the maximum pixel value in kBq/mL within a sphere and A_{true} the FDG activity in kBq/mL within the sphere at the time of acquisition.

In order to check whether the variance between the resulting RC curves of the 6 systems was as small as possible, depending on the chosen reconstruction settings, the PV_{max} of the largest sphere was assumed to be equal to the true activity concentration A_{true} at the start of acquisition and the PV_{max} of the other 5 spheres were scaled to this assumption. The absolute deviation (D) of the RC_{max} per sphere per PET system from the average RC_{max} between all 6 PET systems was determined with the following equation:

$$D = \frac{[RC_{max,x} - RC_{max,a}]}{RC_{max,a}} \cdot 100\%$$

$RC_{max,x}$ represents the RC_{max} of the relevant sphere of one of the 6 PET systems and $RC_{max,a}$ represents the average RC_{max} of the sphere between all 6 PET systems. In addition, the average of all 6 absolute deviations was determined per sphere ($D_{average}$). RC_{mean} was determined by means of a VOI at 50% of the PV_{max} corrected for background uptake (2). The corrected VOI was determined with the following equation:

$$T_{VOI} = \frac{0.5 \cdot (PV_{max} - BG) + BG}{PVmax} \cdot 100\%$$

T_{VOI} is the corrected threshold of the VOI and *BG* is the FDG uptake in the background compartment in kBq/mL. Within this VOI, the mean pixel value was determined and RC_{mean} was then calculated by the following equation:

$$RC_{mean} = \frac{PV_{mean}}{PV_{max}}$$

The absolute deviation of the RC_{mean} per sphere per PET system from the average RC_{mean} between all 6 PET systems was determined in a similar way as for the RC_{max} deviation. Once the reconstruction settings were chosen and the RCs for all spheres were within the acceptable range as defined by EARL (23), additional reconstructions were performed for shorter scan durations (22). For each PET system, the effective scan durations of all reconstructed images are displayed in Table 1. For each reconstructed image the coefficient of variation (COV) was determined and related to the scan durations by means of a power-law fit:

$$COV = a \cdot T^{-b}$$

In this formula *T* is a certain scan duration in seconds (s) with *a* and *b* as fit parameters (22). Phantom data of the Biograph Vision were made available to us and consisted of just one scan with scan duration of 10 minutes. Therefore, exponential decline was assumed with *b* = 0.5. The minimal scan duration (T_{min}) can be derived using the following equation:

$$T_{min} = (\frac{a}{COV_{max}})^{\frac{1}{b}} \cdot \frac{B_{true}}{2.0}$$

B_{true} is the true FDG activity concentration in the background compartment of the phantom at the start of acquisition (22). A maximum COV (COV_{max}) of 0.15 is proposed for the calculation of the minimal scan time (21). If, at this minimal scan duration, the RCs were still within EARL accreditation specifications, T_{min} was introduced into the following equation (22):

$$A \cdot t = 0.0533 \cdot w^2 \cdot T_{min}$$

Within this equation *A* is the FDG activity to administer in MBq, *t* is the time per bed position in seconds (s), and *w* is the body weight in kilograms (kg). Once T_{min} was known, there was only one remaining variable per PET system as shown in the following equation:

$$A \cdot t = C_{sys} \cdot w^2$$

This variable was called the "System Constant" (C_{sys}). C_{sys} of the 6 PET systems were related to the so-called "effective sensitivity" (S_e) per PET system, which was derived from the NEMA specifications with the following equation:

$$S_e = \frac{S_i}{\Delta t}$$

Within this equation S_i is the intrinsic sensitivity at the center of the VOI of the PET system in kcps/MBq and Δt the timing resolution in picoseconds (ps). For each PET system S_i, Δt and S_e specifications are shown in Table 3.

Table 3: The NEMA specifications per PET system (13,31). The effective sensitivity (S_e) is derived from the intrinsic sensitivity at center (S_i) and the timing resolution (Δt) by $S_i/\Delta t$.

Manufacturer	**Philips**		**GE**		**Siemens**	
PET/CT system	Ingenuity TF	Vereos	Discovery D690	Discovery MI	Biograph mCT TrueV	Biograph Vision
Photodetector	PMT	SiPM	PMT	SiPM	PMT	SiPM
S_i at center (kcps/MBq)	7.4	5.7	7.1	13.5	9.6	14.9
Δt (ps)	495	345	544	385	540	249
S_e (cps/MBq/ps)	14.9	16.5	13.1	35.1	17.8	59.8

We determined a power-law fit, which described the C_{sys} as function of the S_E in the following way:

$$C_{sys} = a \cdot S_e^{-b}$$

Finally, this equation was combined with the definition of a body-weight-dependent formula for the product of FDG activity and scan time per bed position to determine a prediction model, as follows:

$$A \cdot t = a \cdot S_e^{-b} \cdot w^2$$

Results

Figure 1 shows the resulting reconstructed images of the IQ phantom of all 6 included PET systems. Due to variation in the positioning of the spheres in the phantom, the spheres in Figures D and F are located differently. Other than that the image quality of the 6 phantom images is visually quite comparable.

The RC curves of all 6 PET systems are shown in Figure 2. All RCs are well within the range of the EARL accreditation specification. The average deviations of the 6 RC curves per sphere are summarized in Table 4. By adjusting the reconstruction settings, the average deviation of the RCmax curves changed from 2.9±1.9% to 2.4±1.7% and the average deviation of the RCmean curves changed from 3.1±1.6% to 2.8±1.5%.

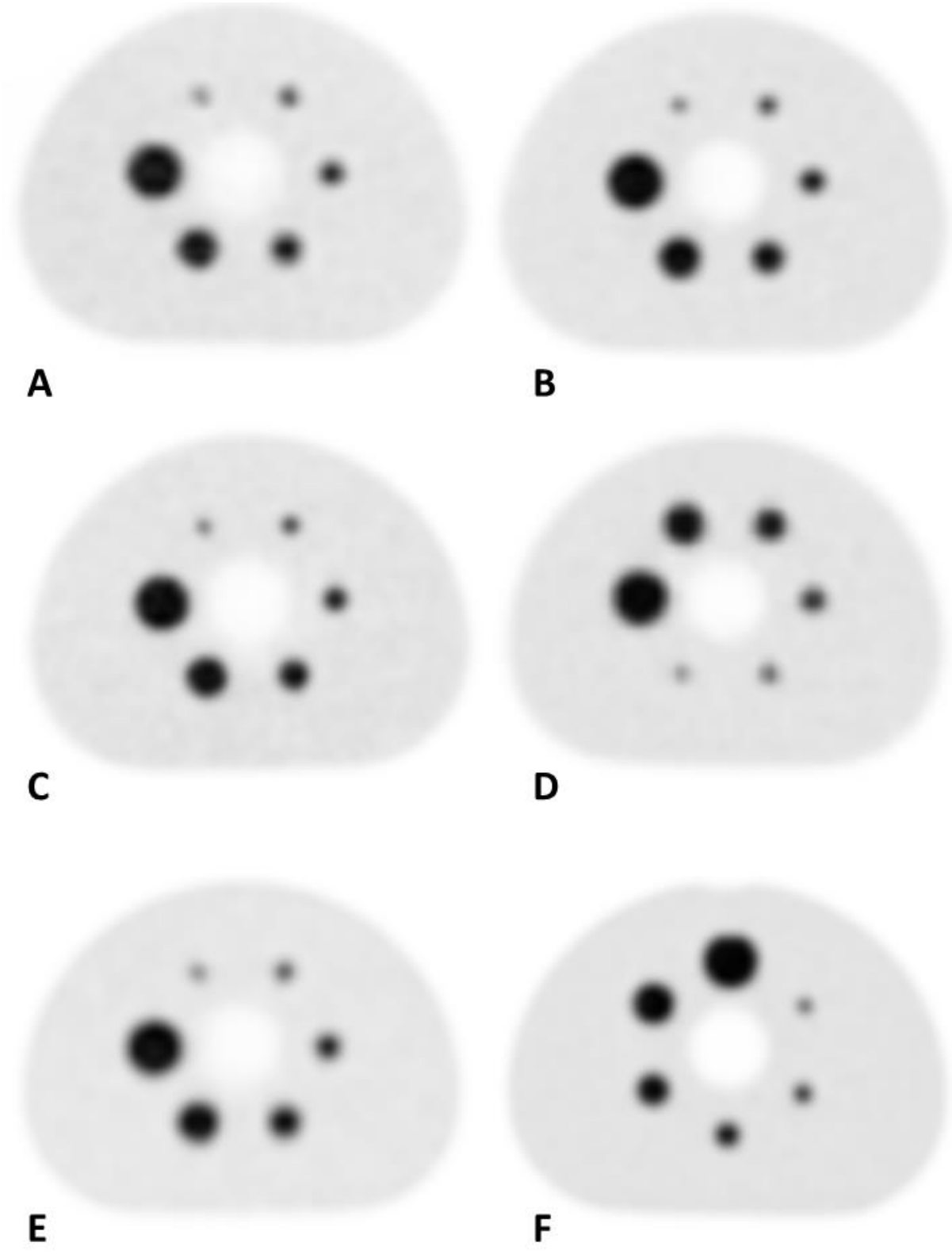

Figure 1: The reconstructed PET images for the Ingenuity (A), Vereos (B), Discovery D690 (C), Discovery MI (D), Biograph mCT TrueV (E), and Biograph Vision (F) at 10 minutes scan duration.

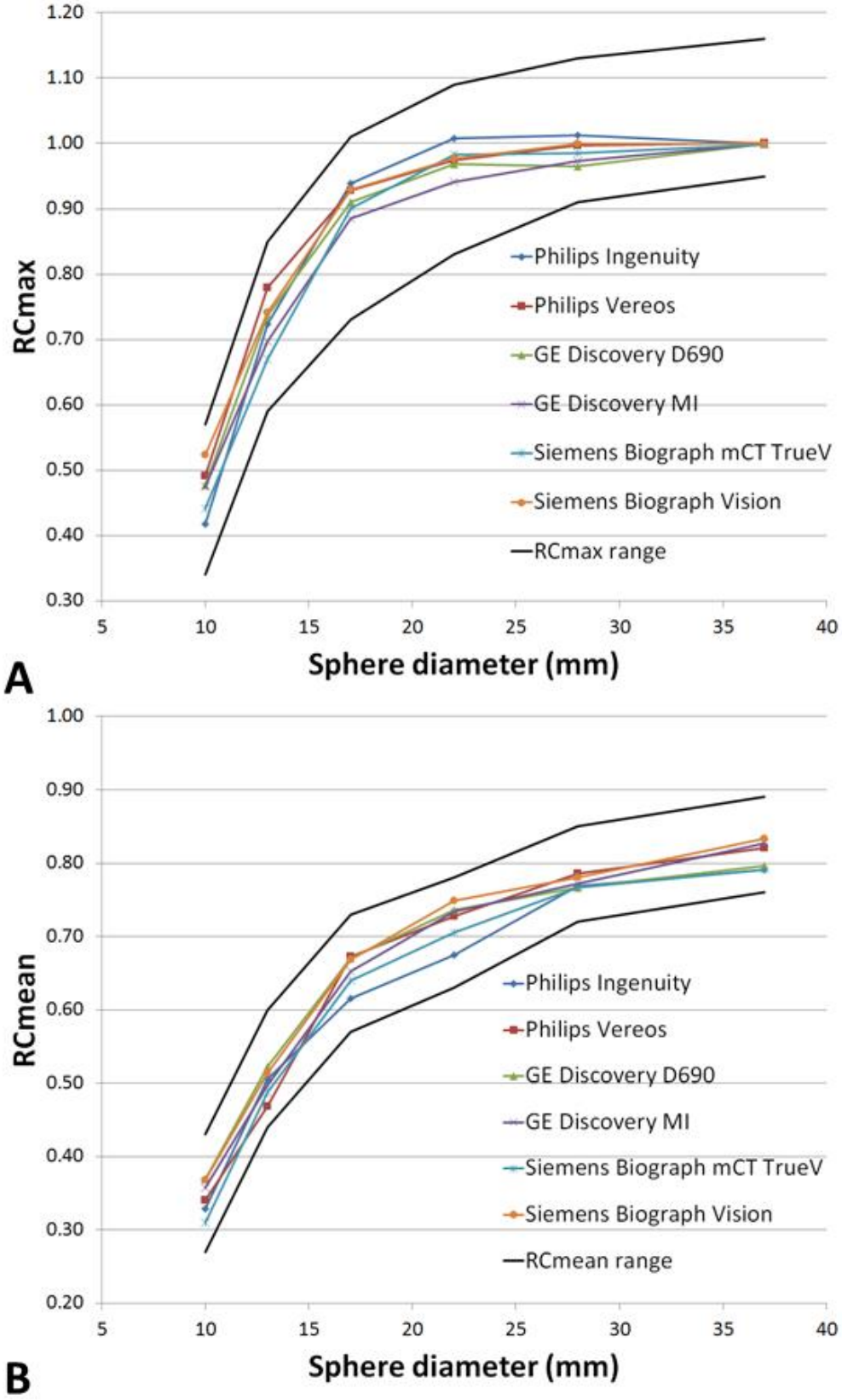

Figure 2: RC_{max} (A) and RC_{mean} curves for all six PET systems, using adjusted EARL reconstruction settings. All RC's were well within EARL specifications.

Table 4: The average deviation of the 6 RC curves per sphere. By adjusting the reconstruction settings, the average deviation of the RC_{max} curves changed from 2.9±1.9% to 2.4±1.7% and the average deviation of the RC_{mean} curves changed from 3.1±1.6% to 2.8±1.5%. The average deviation of the three largest and three smallest spheres are mentioned separately.

	Rcmax				Rcmean			
	Original EARL settings		Adjusted settings		Original EARL settings		Adjusted settings	
Sphere diameter (mm)	$D_{average}$	SD	$D_{average}$	SD	$D_{average}$	SD	$D_{average}$	SD
37	0.1%	0.1%	0.1%	0.0%	1.8%	1.1%	2.1%	0.5%
28	1.7%	1.2%	1.5%	0.8%	0.8%	0.4%	0.8%	0.4%
22	1.9%	1.0%	1.4%	1.4%	3.3%	1.7%	2.8%	1.8%
Average large spheres	1.2%	0.7%	1.0%	0.7%	1.9%	1.0%	1.9%	0.9%
17	1.5%	0.9%	1.8%	0.9%	3.0%	1.2%	2.6%	1.7%
13	4.2%	3.7%	3.8%	2.9%	3.6%	2.0%	3.0%	2.0%
10	7.9%	4.8%	5.9%	4.2%	6.4%	3.2%	5.6%	2.8%
Average small spheres	4.6%	3.2%	3.9%	2.7%	4.3%	2.1%	3.7%	2.1%
Average overall	2.9%	1.9%	2.4%	1.7%	3.1%	1.6%	2.8%	1.5%

In Figure 3, the power-law fits of the COVs in de background compartment are presented as a function of the scan duration. The values of the power-law fit parameters (*a* and *b*), the resulting minimal scan times (T_{min}), and Csys are shown in Table 5. C_{sys} of each PET system is plotted against their S_e in Figure 4. C_{sys} decreases with increasing S_e.

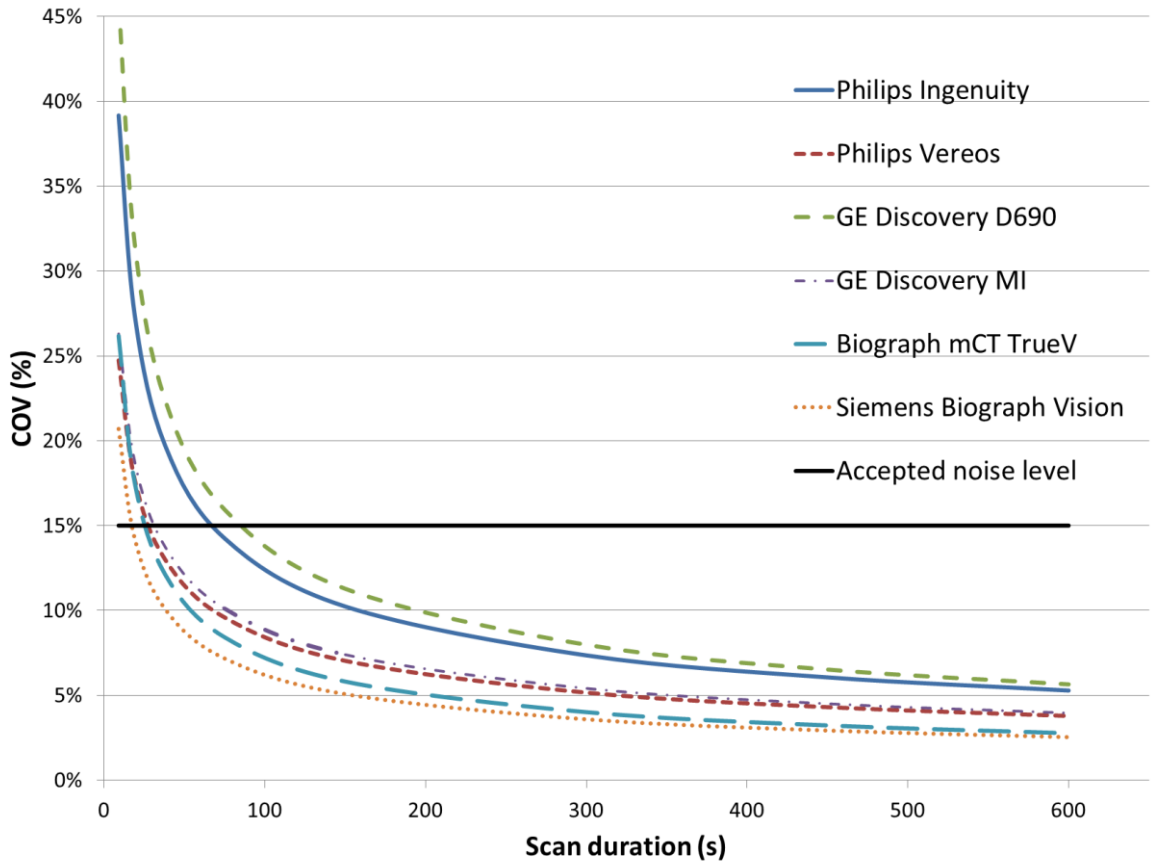

Figure 3: The power-law fits of all 6 PET systems. The accepted noise level is set at 15% (23).

Table 5: The power-law fits resulted in the parameters *a* and *b* with a coefficient of determination (R^2), which indicates how well the trend line fits the data. Using COV_{max}, the resulting T_{min} per PET system is displayed. With the Siemens Biograph Vision, the *b* parameter is fixed on 0.5 and there is no R^2 because the curve is based on only one scan duration.

		a	b	R²	Tmin (s)	System Constant
Philips	Ingenuity TF	1.117	0.477	0.995	61	3.27
	Vereos	0.660	0.447	0.990	40	2.12
GE	Discovery D690	1.374	0.499	0.997	60	3.18
	Discovery MI	0.709	0.451	0.984	33	1.75
Siemens	Biograph mCT TrueV	0.848	0.535	0.987	38	2.02
	Biograph Vision	0.621	0.500	-	26	1.36

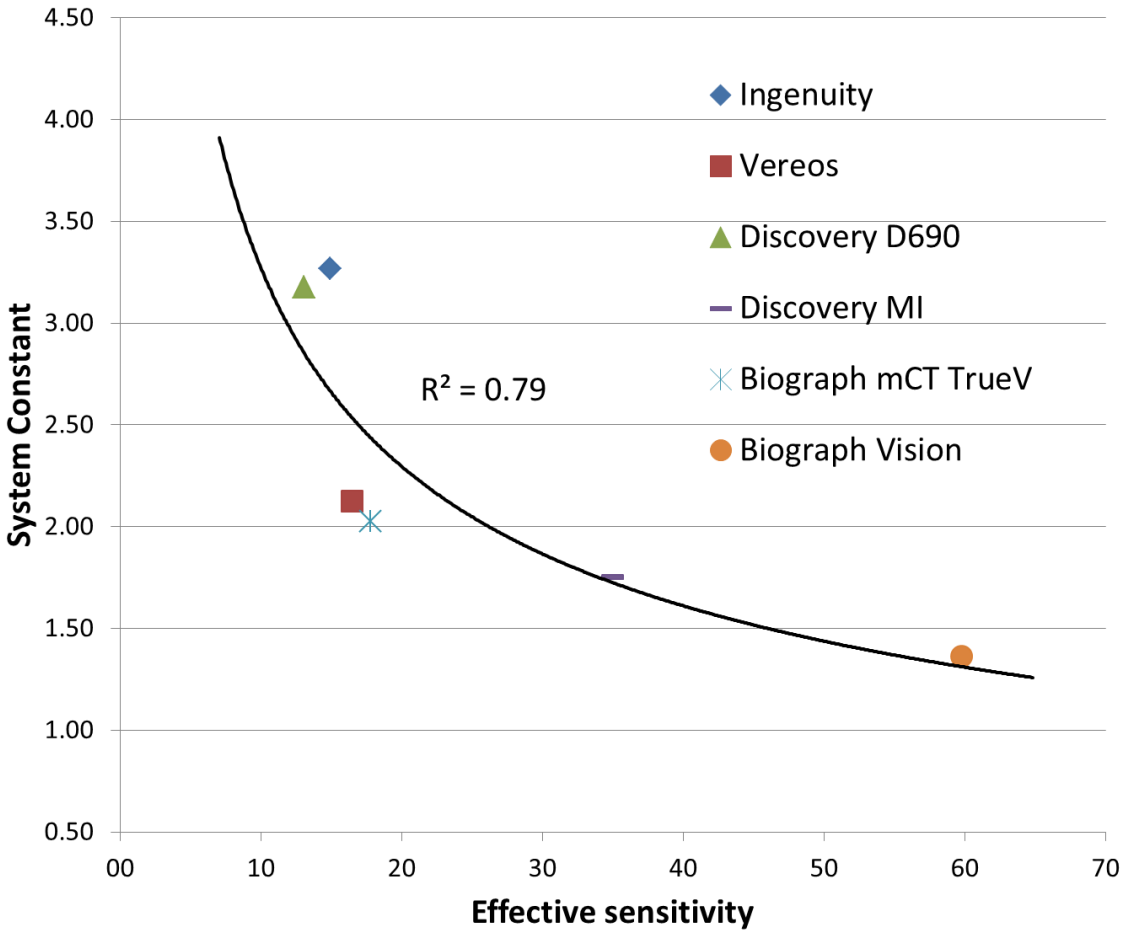

Figure 4: C_{sys} of each PET system plotted against their S_e. A power-law fit is included (R^2 = 0.79).

A power-law fit in Figure 4 describes the relation between C_{sys} and S_e with R^2 = 0.79 and the following formula:

$$C_{sys} = 10.62 \cdot S_e^{-0.51}$$

This leads to the following body-weight dependent formula for the product of FDG activity to administer and scan time per bed position, applicable to any given PET/CT system:

$$A \cdot t = 10.62 \cdot S_e^{-0.51} \cdot w^2$$

Discussion

In this study, the development of a model that predicts the required FDG activity and scan time per bed position for a standardized image quality was demonstrated. The resulting model was based on a strong correlation between the so-called “System Constant” (C_{sys}) and the effective sensitivity (S_e) of a given PET system ($R^2 = 0.79$). The System Constant determines what the patient-specific FDG activity formula is while complying with EARL accreditation specifications and the effective sensitivity depends on the NEMA specifications of the respective PET system. The lower the C_{sys}, the lower the combination of administered FDG activity and scan duration per bed position needs to be in order to ensure a standardized image quality while complying with EARL accreditation specifications. An interesting finding is that there are large differences between PET systems as expressed in the C_{sys}. varying up to a factor of 2.4. As expected, the dPET systems (Vereos, Discovery MI, and Vision) are associated with a lower C_{sys} than the cPET systems of the same manufacturer (Ingenuity, Discovery D690, and Vision respectively). However, a dPET system does not necessarily have a lower C_{sys} than all cPET systems, because the C_{sys} of the Vereos is higher than the C_{sys} of the Biograph mCT TrueV.

The advantage of using S_e as characteristic of a PET system is that it can be determined relatively easily based on the NEMA specifications, which are publicly known for a PET/CT system currently on the market. However, the correlation between C_{sys} and S_e is not perfect, which may be due to the fact that other factors that affect image quality, such as scatter, random coincidences, field of view (FOV), and the chosen number of iterations were not taken into account (32). The noise equivalent count (NEC) definition as described by Surti et al. does include scatter and random coincidences into the calculation of the effective sensitivity (32). This definition is, however, is not necessarily a good predictor either when using OSEM reconstruction settings (33). Hence, the chosen number of iterations quite possibly has an important effect on the correlation between C_{sys} and our defined effective sensitivity (32,33), which may be improved by using reconstruction settings with a comparable number of iterations.

No margin of error is displayed in the visualization of the correlation between C_{sys} and S_e (Figure 4). However, measurement errors have most likely been made in, for example, determining the start time of the acquisition and the activity concentration at a certain time. In addition, there was no data available for the Siemens Vision at shorter scan durations, so that the minimum required scan time, from which the C_{sys} is derived, is not determined as accurately as recommended by Koopman et al. (22). Furthermore, we did not adjust or test the original EARL reconstruction settings for a small variance in RC curves when we started this study. Only when more data was added from other PET/CT systems did we test several reconstruction settings and compare them with the data we had already collected (see Appendix A.1) Adjusting the reconstruction settings does, however, have an effect on the outcomes. For example, if all original EARL reconstruction settings had been used R^2 would have been 0.71 instead of 0.79 and the model would change (see Appendix A.2). Finally, the NEMA specifications as described by Vos et al. (13) were used to derive the S_e of the six PET systems. However, Sluis et al. have determined a different intrinsic sensitivity and temporal resolution for the Siemens Biograph Vision PET system (34), causing the S_e to be even higher than initially assumed in our study. Furthermore, Zhang et al. have described alternative specifications for the other five PET systems, because other sources were

consulted (35). Within studies of performance, the specifications of intrinsic sensitivity and temporal resolution often turn out to be even better than initially issued by manufacturers. By applying the NEMA specifications as indicated by Sluis et al. and Zhang et al, the correlation between C_{sys} and S_e increases to a R^2 of 0.85 (see Appendix A.3). Nevertheless, the results of this study suggest that our prediction model could be a valuable tool in the future to estimate a weight-dependent formula for the required FDG activity and scan time per bed position for a PET system with which no clinical experience has yet been gained.

Conclusion

We have developed a prediction model, based on the strong correlation between the so-called “System Constant” and the effective sensitivity of a given PET system. This System Constant determines what the patient-specific FDG activity formula is while complying with EARL accreditation specifications. The large differences between PET systems, which currently dominate the market, imply large differences in this System Constant, which directly influences clinical routine and costs per patient. In the future, the prediction model is therefore an important tool to use for the comparison between multiple PET systems when purchasing a new PET system.

CHAPTER III

Value of ultra-high resolution reconstructions in small lesion detection with digital PET

Abstract

BACKGROUND: With digital PET technology spatial and temporal resolution has increased, thereby possibly improving small lesion detection. The use of small voxel reconstructions may enable improved small lesion detection with digital PET. Therefore, our aim was to evaluate the potential value of ultra-high-resolution (uHR) reconstructions in digital PET imaging to improve small lesion detection, compared to high-resolution (HR) reconstructions, in patients with cancer.

METHOD: Two nuclear medicine physicians performed a blinded side-by-side comparison between HR and uHR reconstructed images, which were randomly placed left and right. Based on image contrast, noise, and diagnostic confidence, the nuclear medicine physicians stated their preference. In case of disagreement, a third nuclear medicine physician was consulted. For each lesion, SUV_{max}, SUV_{mean}, lesion volume, and lesion-to-background ratio were determined in both HR and uHR reconstructions. For each image, the noise level, SNR_{max}, and SNR_{mean} were determined.

RESULTS: Lesion volume decreased with 37% ($P < 0.001$), SUV_{max}, SUV_{mean}, and lesion-to-background ratio increased with 12%, 12%, and 10% respectively ($P < 0.001$). The noise level increased with 11% ($P < 0.001$) and SNR_{max} and SNR_{mean} did not change significantly. Visually, there was no preference for the uHR or HR reconstruction.

CONCLUSION: Small lesion detection is less hampered by the partial-volume effect within uHR reconstructions as compared to HR reconstructions. However, we do not expect the quantitative change between HR and uHR reconstructions in digital PET to be relevant for the purpose of FDG-PET in current clinical practice.

Introduction

Cancer is one of the most common diseases of our time. In patients with suspected malignancies both prognosis and therapeutic management particularly depend on the tumor stage. Early detection and accurate diagnosis are therefore essential. FDG-PET is frequently used for diagnosing, staging, restaging and therapy response assessment. Gambhir et al. estimated the average FDG-PET sensitivity and specificity at 84% and 88% respectively (36). The two main limitations of PET are the relatively low spatial resolution and the generally low signal-to-noise ratio (SNR) (37). The low spatial resolution introduces the partial-volume effect (PVE). The PVE limits correct quantitative measurements of small lesions, because they are overestimated in size and underestimated in FDG uptake due to spill out of activity (38). This also decreases the sensitivity for small lesions (13). In recent years, there have been multiple advances in PET/CT that potentially improve cancer imaging and small lesion detection. As PET technology progresses and spatial and temporal resolution of new digital systems increase, manufacturers provide new reconstruction possibilities. Improved small lesion detection is enabled e.g. by using smaller voxels, PSF modeling or less post-filtering in the image reconstruction (13).

The Isala Department of Nuclear Medicine currently retains a Vereos PET/CT system (Philips Healthcare), which is a dPET. To meet the current EARL accreditation specifications for FDG-PET imaging with this system, the use of relatively large 4x4x4 mm^3 voxels is recommended (15). The use of large voxels results in more counts per voxel and subsequently in a reduction of image noise as compared to the use of small voxels. However, large voxels also enhance the PVE. Koopman et al. have shown that the detection of small lesions on a state-of-the-art TOF PET/CT-scanner can be improved using 2x2x2 mm^3 voxel (high resolution) reconstructions (15,39) and this has already been incorporated into the clinical practice of the Isala Department of Nuclear Medicine. In addition, the Vereos provides the possibility to use 1x1x1 mm^3 voxel (ultra-high resolution) reconstructions. A phantom study has shown that this ultra-high resolution (uHR) reconstruction has the potential to improve the detection of small lesions even more (15), but it has not yet been investigated whether this applies to patient data as well and how nuclear medicine physicians evaluate these uHR PET-images in clinical practice. An illustration of the effect of voxel-size on the imaged lesion parameters is shown in Figure 1.

Our aim was to evaluate the potential value of ultra-high-resolution (uHR) reconstructions in digital PET imaging to improve small lesion detection, compared to high-resolution (HR) reconstructions, in patients with cancer.

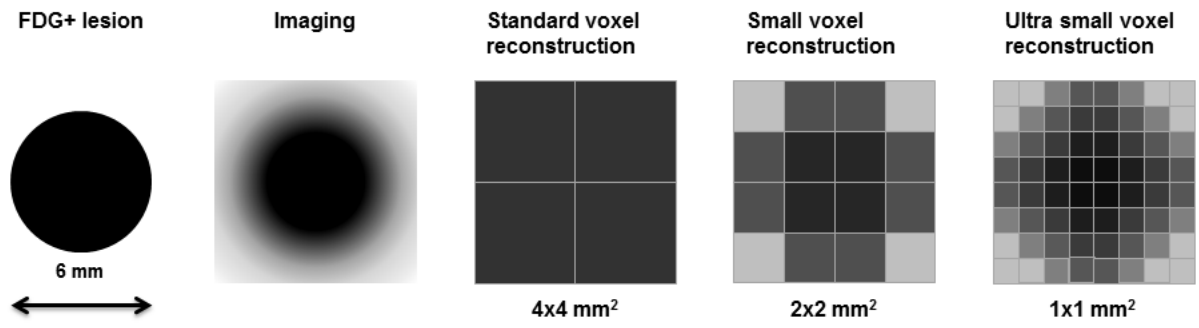

Figure 1: An illustration of the effect of voxel-size on the imaging of lesion parameters.

Methods

To investigate the potential value of uHR reconstructions on small lesion detectability using a digital PET system, we have performed a patient study.

Study population

We retrospectively included 31 patients who participated in the PETPET-study and underwent FDG-PET/CT first on dPET. Patients signed a written informed consent form, and this study was approved by the local medical ethics committee (METC, Isala). Only patients who have at least one FDG positive lesion and a homogeneous liver on at least three slices were selected for this study. Patients fasted for at least 6 hours before scanning. Blood glucose levels were measured prior to intravenous injection of FDG to ensure a value below 15 mmol/L. A dedicated dose protocol, depending quadratically on a patient's body weight, was used. This protocol is described by the formula $A \cdot t = 6.22 \cdot w^2$, where "A" is the FDG activity to administer (in MBq), "t" the time per bed position (in seconds) and "w" is the patient's body weight (in kilogram).

Data Acquisition

All PET/CT scans were acquired with the Vereos PET/CT system (Philips Healthcare). This digital photon counting TOF scanner is combined with a 128-channel CT system. The PET detector ring consists of 18 detector modules, each containing a 40x32 array of 4x4x19 mm^3 LYSO crystals, which are individually coupled to SiPM detectors. The TOF performance is defined by a timing resolution of 345 picoseconds and a localization accuracy of 5.2 cm. PET/CT acquisitions started with a CT scan for attenuation correction, followed by a PET scan. The scan duration was either 72 seconds or 144 seconds per bed position, respectively for patients with body weight ≤80 kg and >80 kg. Administered FDG activity ranged from 216 to 600 MBq.

Data Reconstruction

PET data were reconstructed using a list-mode OSEM+TOF algorithm without PSF modeling. Images were reconstructed in two types of matrices: 288x288 matrices with voxel size 2x2x2 mm^3 (HR) and 576x576 matrices with voxel size 1x1x1 mm^3 (uHR). For both types of voxel reconstructions, 3 iterations were applied and respectively 17 and 9 subsets.

Data analysis

Integrated PET/CT data were visually analyzed on a dedicated workstation (Sectra Workstation IDS7, Sectra AB, Sweden). Initially, two experienced nuclear medicine physicians (NP1 and NP2) performed a blinded side-by-side analysis of the HR and uHR reconstructed images, which were randomly placed left and right. Based on image contrast, image noise, and diagnostic confidence, the nuclear medicine physicians were asked to state their preference. They answered the three questions with either "left" or "right" or "no preference". In case of disagreement between the two nuclear medicine physicians a third nuclear medicine physician (NP3) was asked to perform the side-by-side analysis as well and to make a choice between the answers of the first two nuclear medicine physicians.

Quantitative measurements were performed on a dedicated workstation (IntelliSpace Portal, Philips Healthcare). Lesions were selected on the HR reconstructed image. Only lesions with measurable FDG uptake, located in the thorax, high abdominal region or skeleton, were included for analysis. A maximum of 5 lesions per patient was incorporated to prevent a

possible bias if some patients had many small lesions. In these cases, the 5 smallest lesions were selected. The attenuation CT scan was used to identify the location of the lesions.

For each lesion, we measured the maximum and mean standardized uptake values (SUV_{max} and SUV_{mean}, respectively) in both HR and uHR reconstructed images. The SUV_{mean} and lesion volume were calculated from a 3D isocontour at 70% of the maximum pixel value. Lesions with a volume > 10 mL were excluded to limit the analysis to small lesions. In addition, we calculated the lesion-to-background ratio (LB_{ratio}), defined as the ratio between the lesion SUV_{max} and the SUV_{mean} in the immediate background of the lesion (SUV_{mean_B}). To measure the SUV_{mean_B} we defined a region of interest (ROI_L) on an axial plane that closely fitted the lesion and a second region of interest (ROI_{LB}) that enclosed both the lesion and a surrounding background area of approximately 800 mm^2. To calculate SUV_{mean_B} the following equation was used:

$$SUV_{mean\_B} = \frac{(SUV_{mean\_LB} \cdot ROI_{LB}) - (SUV_{mean\_L} \cdot ROI_L)}{ROI_{LB} - ROI_L}$$

Furthermore, we performed background measurements in the liver on both HR and uHR reconstructed images, by drawing three ROIs of approximately 900 mm^2 on three axial slices in homogeneous areas. The SUV_{mean} and standard deviation (SD) of all nine ROIs were averaged to determine the noise level of the image with the following equation:

$$Noise = \frac{SD_{liver}}{SUV_{mean\_liver}}$$

Subsequently, we calculated the maximum and mean SNR (SNR_{max} and SNR_{mean}, respectively) using the following equation:

$$SNR = \frac{SUV}{SD_{liver}}$$

Within this equation the SUV_{max} was used in case of SNR_{max} calculation and the SUV_{mean} in case of SNR_{mean} calculation. For all parameters (lesion volume, SUVs, LB_{ratio}, background noise, and SNRs), the relative changes between the HR and uHR reconstructed images were determined with the following equation:

$$Relative\ change = \frac{P_{uHR} - P_{HR}}{P_{HR}} \cdot 100\%$$

In this equation, *"P"* can be replaced by each of the mentioned parameters.

Statistical Analysis

We used the Wilcoxon signed-rank test to compare visual preferences regarding contrast, noise, and diagnostic certainty between the first two nuclear medicine physicians. In the same way the visual preferences by NP3 were compared to NP1 and NP2. The same test was used to compare volume, SUV_{max}, SUV_{mean}, LB_{ratio}, SNR_{max}, SNR_{mean}, and noise measurements between the HR and uHR reconstructions. Furthermore we performed linear regression analysis by means of the F test and Pearson correlation coefficients to determine correlations between lesion volume and relative changes in SUV_{max}, SUV_{mean}, LB_{ratio}, SNR_{max}, and SNR_{mean}. A P-value of less than 0.05 was considered to indicate statistical significance.

Results

Patient characteristics

Clinical data from 31 patients are shown in Table 1. Initially, 114 lesions were included. Two lesions were excluded because they had a volume of > 10 mL on both reconstructed images.

Table 1: General patient- and lesion characteristics.

Patient characteristics (n = 31)		
Gender		
	Female	13
	Male	18
Age (years)		65 ± 11
Body weight (kg)		79 ± 15
Glucose (mmol/L)		5.5 ± 0.9
Proven malignancy		
	Yes	23
	No	5
	Unknown	3
Lesion characteristics (n = 112)		
Type		
	Primary tumor	22
	Lymph node	41
	Metastasis	49

Quantitative data analysis

The quantitative results are shown in Table 2 and the relative change between the HR and uHR reconstructed images is shown in Table 3. The average lesion volume was significantly smaller on the uHR reconstructed images than on the HR reconstructed images ($P < 0.001$). Histograms of the lesion volume in both HR and uHR reconstructions, visualizing the shift to more small lesions in the uHR reconstruction, are shown in Figure 2. The average background noise, SUV_{max}, SUV_{mean}, and LB_{ratio} were significantly higher on the uHR reconstructed images than on the HR reconstructed images ($P < 0.001$). The SNR_{max} and SNR_{mean} did not change significantly between HR and uHR reconstructions ($P = 0.897$ and $P = 0.918$ respectively).

We have found minimal correlations between lesion volume (uHR) and relative changes in SUV_{max}, LB_{ratio}, and SNR_{max} with Pearson correlation coefficients of -0.08, -0.12, and -0.04. All these correlations were non-significant ($P = 0.39$, $P = 0.23$, and $P = 0.66$ respectively). The correlation between lesion volume (uHR) and relative changes in SUV_{mean} and SNR_{mean} were moderate but significant, with Pearson correlation coefficients of -0.37 ($P < 0.001$) and -0.19 ($P < 0.05$) respectively. Relative change in SUV_{mean} when using uHR reconstruction settings instead of HR reconstruction settings is shown in Figure 3.

Table 2: The quantitative results of the lesion measurements in the HR and uHR reconstructed images.

	HR reconstructed image				uHR reconstructed image			
	Min	Max	Mean	SD	Min	Max	Mean	SD
Lesion Volume (mL)	0.1	5.1	0.7	0.9	0.1	5.2	0.5	0.8
Background Noise (%)	11.6	19.0	15.6	1.9	13.7	21.8	17.2	2.2
SUVmax	2.2	29.9	6.1	3.8	2.6	32.0	6.8	4.3
SUVmean	1.7	19.9	4.7	2.9	2.1	20.1	5.2	3.1
LBratio	2.5	21.1	5.2	2.9	1.5	22.6	5.8	3.5
SNRmax	5.5	59.8	16.0	8.7	4.3	64.0	16.0	9.6
SNRmean	4.3	39.8	12.4	6.7	3.5	44.3	12.4	7.1

Table 3: The relative change between the measured lesion parameters in the HR and the uHR reconstruction. The result of the significance test of the relative change is displayed in the last column.

	Relative change				
	Min	Max	Mean	SD	P-value
Lesion Volume (mL)	-88.4%	54.6%	-37.0%	26.1%	< 0.001
Background Noise (%)	-2.6%	26.4%	10.6%	6.5%	< 0.001
SUVmax	-19.6%	33.3%	11.5%	8.4%	< 0.001
SUVmean	-7.1%	38.1%	11.9%	8.4%	< 0.001
LBratio	-51.2%	58.1%	10.2%	14.3%	< 0.001
SNRmax	-25.0%	33.3%	0.3%	14.2%	0.897
SNRmean	-23.5%	38.1%	0.6%	14.6%	0.918

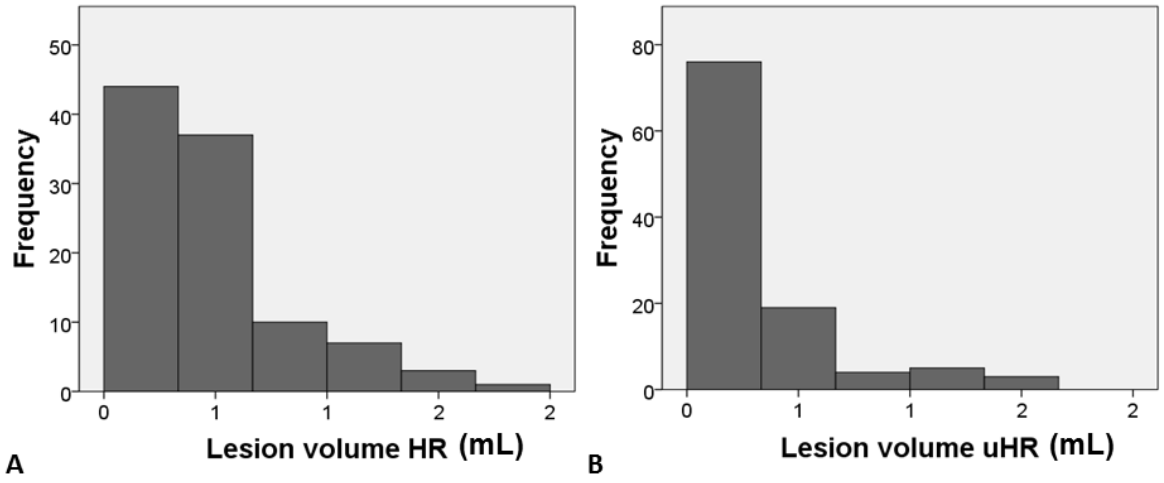

Figure 2: Two histograms visualizing the frequency of certain lesion volumes in the HR (A) and uHR (B) reconstructed images. When uHR reconstruction settings are used instead of HR reconstruction settings, there is a shift towards smaller lesion sizes.

Two visual examples of lesions in both HR and uHR reconstructions are shown in Figure 4 and 5. The quantitative change of all lesion parameters between both reconstructions for the two examples is shown in Table 4. Both visually and quantitatively, the uHR reconstruction has a positive effect on lesion X. The lesion volume decreases and the SNR increases. Due to noise increase, the SNR for lesion Y decreases. Lesion Y is about three times as large as lesion X.

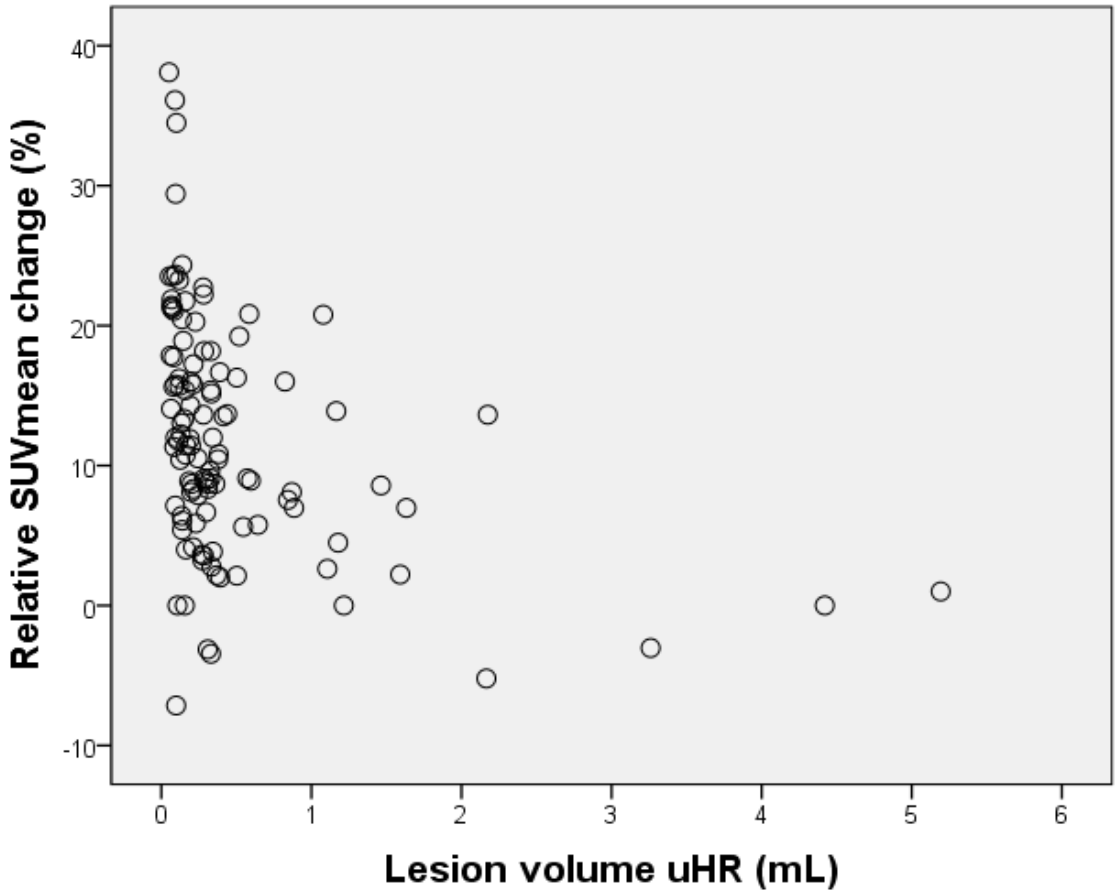

Figure 3: Relative changes in SUV_{mean} for all 112 included lesions using uHR reconstruction settings instead of HR reconstruction settings. For all lesions the SUV_{mean} changed 12% between both reconstructions.

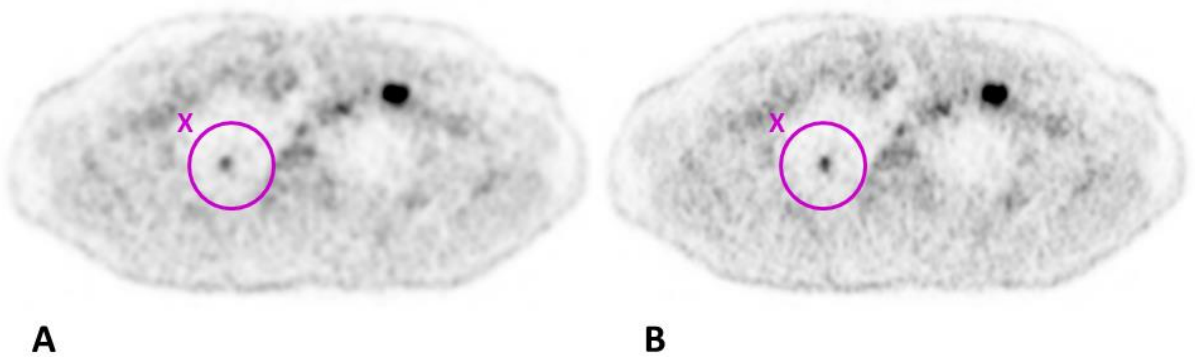

Figure 4: Transverse PET images of a clinical example of a small lesion (X) using both HR reconstruction settings (A) and uHR reconstruction settings (B).

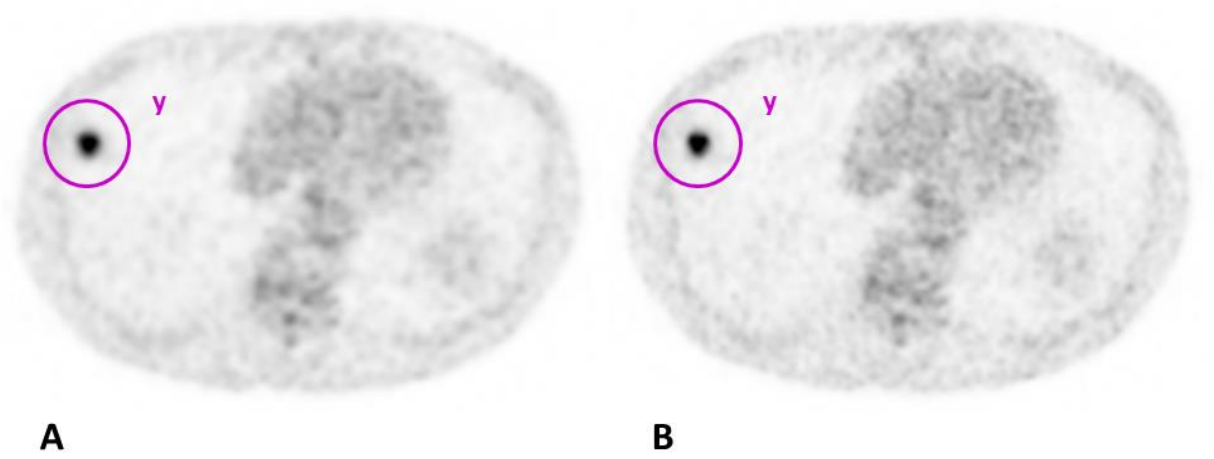

Figure 5: Transverse PET images of a clinical example of a larger lesion (Y) as compared to lesion X using both HR reconstruction settings (A) and uHR reconstruction settings (B).

Table 4: The quantitative change of lesion parameters between HR and uHR reconstructed images of two clinical examples.

	Lesion X			Lesion Y		
	HR	uHR	Relative change	HR	uHR	Relative change
Lesion Volume (mL)	0.2	0.1	-54%	0.6	0.5	-14%
Background Noise (%)	20	20	0%	16	20	27%
SUVmax	4.2	5.6	33%	5.9	5.9	0%
SUVmean	3.4	4.4	29%	4.7	4.8	2%
LBratio	6.3	8.9	41%	9.6	10.5	10%
SNRmax	10.5	14.0	33%	19.7	14.8	-25%
SNRmean	8.5	11.0	29%	15.7	12.0	-23%

Visual data analysis

The preferences of the nuclear physicians regarding contrast, noise and diagnostic certainty between HR and uHR reconstructions are shown in Figure 6. In the categories noise and diagnostic certainty, the preferences of NP1 and NP2 were significantly different ($P < 0.001$). The preferences of the third reader (NP3) also differed significantly from the preferences of NP1 in those two categories ($P < 0.001$). The agreement between all three nuclear medicine physicians regarding contrast level, noise level, and diagnostic certainty was on average 68% (n = 21), 29% (n = 9), and 3% (n = 1) respectively. Figure 6 shows this agreement by means of solid contours. In addition, the dotted lines represent the agreement between NP2 and NP3. Average agreement per category (contrast, noise, and diagnostic certainty) between NP2 and NP3 was 84% (n = 26), 90% (n = 28), and 87% (n = 27) respectively. When looking at corresponding preferences, we see no clear preference in any category for one of the two reconstructed images. In 37% of cases NP2 and NP3, preferred the uHR image in the contrast category and the HR image in the noise category. However, in 34%, the opposite choice was made.

From a total of 31 patients, there were 9 patients where NP2 and NP3 did not have the same preferences based on the three categories of contrast, noise, and diagnostic confidence. Of these 9 cases, there were 8 where in one of the nuclear medicine physicians answered one of the three questions with “no preference”, while the other had made a choice between HR and uHR. Hence, there was only one case where NP2 and NP3 made an opposite choice. The choices of the nuclear medicine physicians in this particular case are shown in Table 5

and the PET images of both reconstructions are shown in Figure 7. Visually, there is no obvious difference between both images. Within this patient one lesion was included for this study, which is circled in Figure 7. Visually, the lesion is slightly sharper on the uHR reconstructed image, but there is not a distinct difference. The lesion is, however, visible on the CT images and quantitatively, there is a relative increase in SUV_{max}, SUV_{mean}, and LB_{ratio} and decrease in lesion volume when uHR reconstruction settings are used instead of HR reconstruction settings, as shown in Table 6.

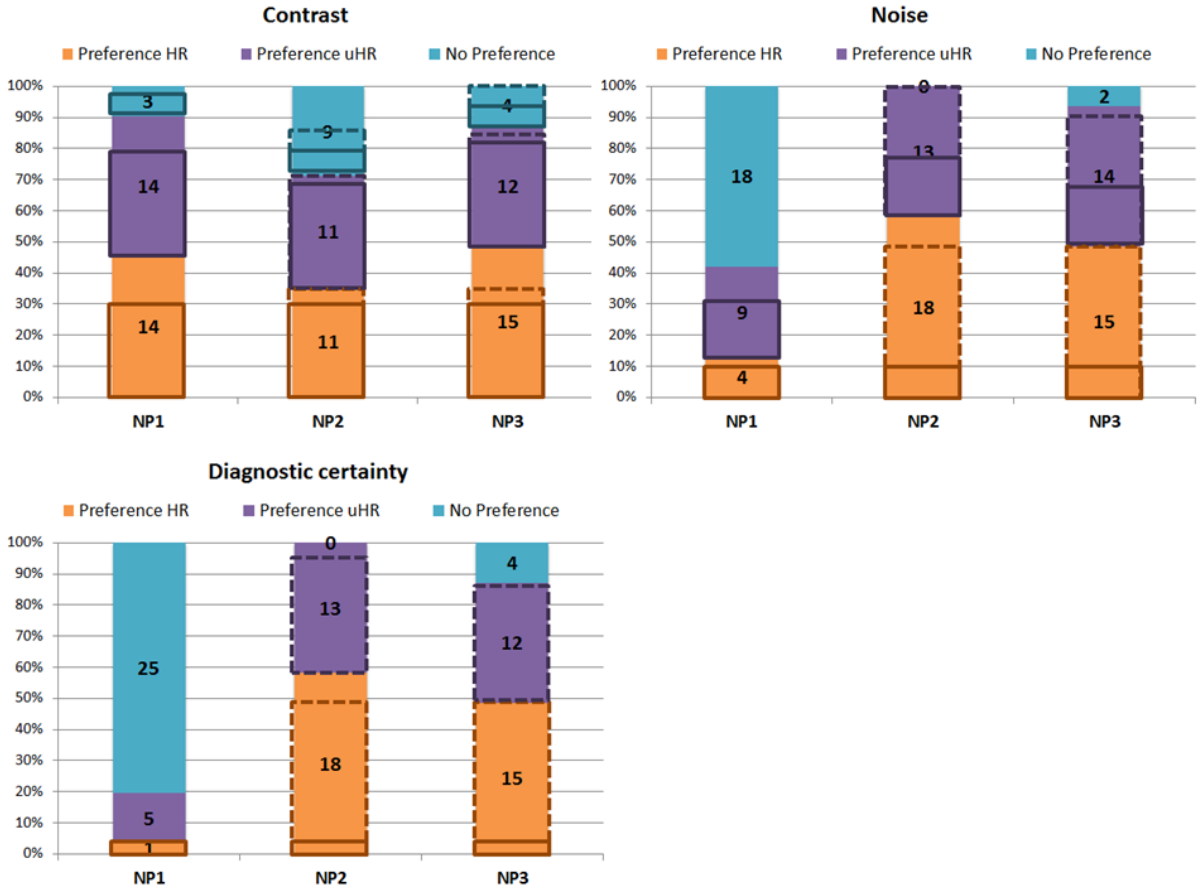

Figure 6: The results of the visual analysis. The solid contours indicate agreement between the three nuclear medicine physicians and the dotted contours indicate agreement between NP2 and NP3.

Table 5: Preference outcomes in the one case where NP2 and NP3 made an opposite choice.

	NP1			**NP2**			**NP3**		
	Contrast	Noise	DC	Contrast	Noise	DC	Contrast	Noise	DC
Preference	HR	uHR	NP	NP	HR	HR	HR	uHR	NP

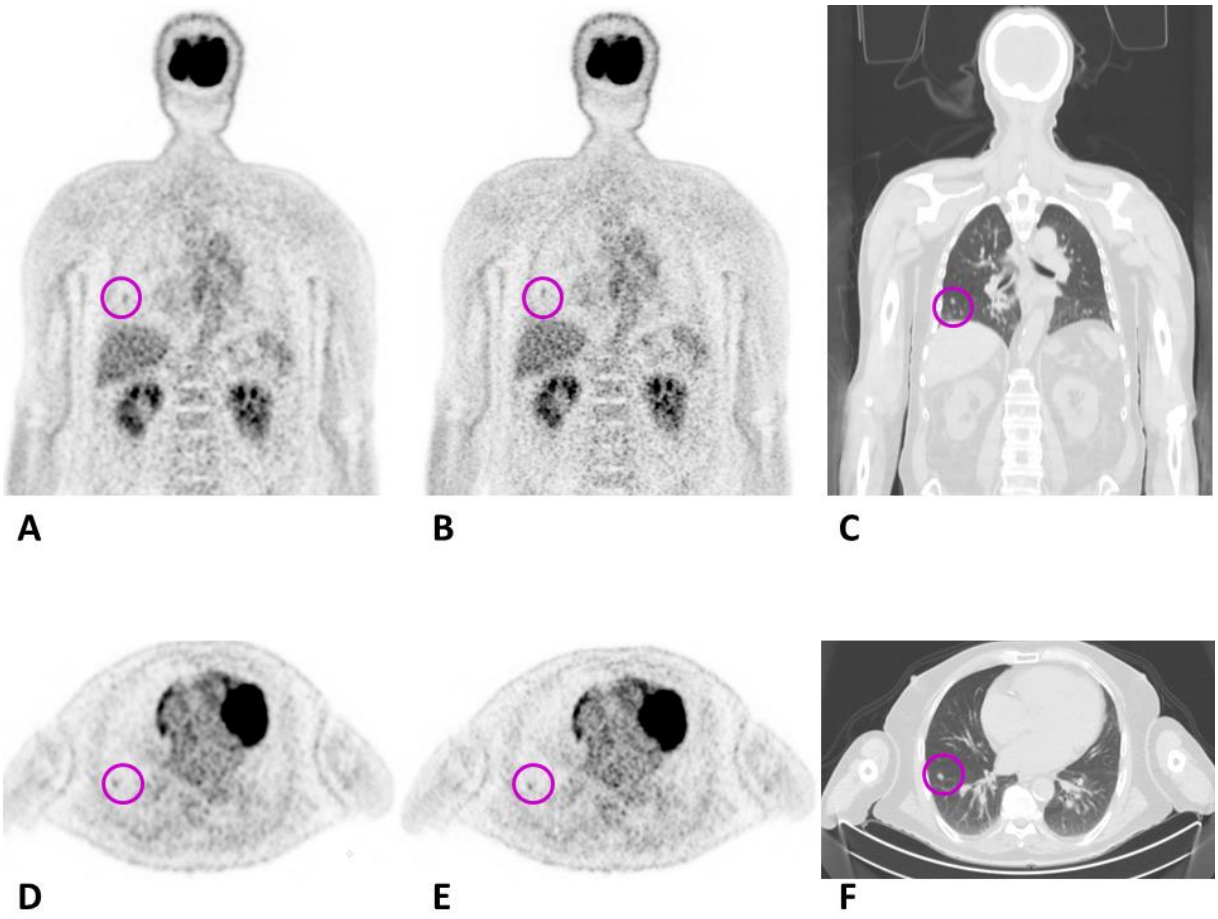

Figure 7: Coronal and transverse PET images using HR reconstruction settings (A + D) and uHR reconstruction settings (B + E) and the CT images (C + F) of the one case where NP2 and NP3 had opposite preferences regarding contrast and noise. The one selected lesion is indicated by the purple circles.

Table 6: Quantitative results of the lesion of Figure 7 summarize relative change of lesion volume, background noise, SUV_{max}, SUV_{mean}, and LB_{ratio} between the HR and uHR reconstructed images.

	HR	uHR	Relative change
Lesion Volume (mL)	0.4	0.1	-80%
Background Noise (%)	17	23	38%
SUVmax	2.2	2.6	18%
SUVmean	1.7	2.1	24%
LBratio	2.9	4.0	37%
SNRmax	5.5	4.3	-21%
SNRmean	4.3	3.5	-18%

Discussion

In this study we evaluated the impact of uHR reconstruction settings on quantitative and visual PET data. We found a significant decrease in lesion volume of 37% ($P < 0.001$) and significant increases in SUV_{max}, SUV_{mean} and lesion-to-background ratio of 12%, 12% and 10% respectively ($P < 0.001$). In addition, as shown in Figure 3, the SUVs are almost always higher in the uHR reconstruction than in the HR reconstruction. The SNR did not change significantly when uHR reconstruction settings were used instead of HR reconstruction settings. SNR measurements in our study for both HR and uHR reconstructions are consistent with the results of Adler et al. (40). As shown in the two examples in Figure 4, Figure 5, and Table 4, the use of uHR reconstruction settings mainly has a positive effect on the visualization and quantification of small lesions. Although quantitatively both the contrast level and the noise level increased significantly in the uHR reconstruction as compared to the HR reconstruction, the nuclear medicine physicians had almost as much preference for the HR reconstruction as for the uHR reconstruction in both categories. In terms of diagnostic certainty, there was no clear preference either for any of the two reconstructions. Hence, both visually and in the SNR measurements there is no significant change between both reconstructions. However, since the lesion volume decreased significantly in the uHR reconstruction and SUVs and lesion-to-background ratio's increased significantly, it can be concluded that the detection of small lesions is less hampered by the PVE when uHR reconstructions are used.

A relevant study was carried out by Koopman et al. for the comparison between reconstructions with voxels of 4x4x4 mm^3 and voxels of 2x2x2 mm^3 (14). In their study, reducing the voxel size resulted in an increase of SNR_{max} by 27% ($P < 0.001$) and SNR_{mean} by 13% ($P = 0.015$). In lesions < 0.75 mL, the SNRs increased to 46% and 23% respectively. In addition, the nuclear medicine physicians in most cases also had a preference for the smaller-voxel reconstruction. Hence, the transition from the 4x4x4 mm^3 to the 2x2x2 mm^3 voxel reconstruction has a greater effect on the small lesion detection than the transition from the 2x2x2 mm^3 (HR) to the 1x1x1 mm^3 (uHR) voxel reconstruction. This could be explained by the suggestion that the limit of the intrinsic reconstructed spatial resolution of the PET / CT system has been reached as described by Moses et al. (41). Should developments in the future improve this, we would recommend re-examining the value of uHR reconstructions.

Patients included in this study received a 20% higher administered FDG activity than normally administered at the Isala department of nuclear medicine. These scans benefit from the most ideal conditions that are currently available at the Isala department of Nuclear Medicine. The disadvantage is that the results can therefore not yet be fully translated into regular clinical practice. Furthermore, we used reconstruction settings as recommended by the manufacturer, for both the HR and the uHR reconstructions. These may not be the most optimal settings and therefore introducing PSF modeling or optimizing the reconstruction settings by changing the number of iterations and subsets may further improve these reconstructions and thereby the detection of small lesions (12,13,15). In addition, we did not use the same number of subsets (17 for the HR and 9 for the uHR reconstruction). If we also used 17 subsets for the uHR reconstruction, both the contrast and the noise level would probably have been higher. It could be that in that case the quantitative difference between HR and uHR reconstructions would increase. However, in order to evaluate the clinical relevance, it should be investigated to what extent the noise level would increase with

respect to the increase in contrast level. Finally, it was beyond the scope of this study to assess the sensitivity and specificity of the uHR reconstruction. All lesion-like areas with measureable FDG uptake were included, even though some were so small that one could argue whether it was noise or a lesion.

Conclusion

A small quantitative increase has been found in the SUVs and lesion-to-background ratio in the uHR reconstruction as compared to the HR reconstruction. In addition, the measured lesion volume decreases significantly. We can therefore conclude that the uHR reconstruction ensures that the small lesion detection is less hampered by the partial-volume effect. However, the signal-to-noise ratio did not change. Therefore, we do not expect these changes to be relevant for the purpose of FDG-PET in current clinical practice. This is also reflected in the visual assessment, where nuclear medicine physicians had no clear preference for the uHR reconstruction. Should the value of exact measurements of lesion parameters increase in the future, then the uHR reconstruction would be useful, but otherwise the potential value of uHR reconstructions in digital PET imaging for the improved detection of small lesions is minimal.

References

1. IKNL. Cijfers over kanker. Nederlandse Kankerregistratie (NKR), IKNL. 2018.

2. Boellaard R, Doherty MJO, Weber WA, Mottaghy FM, Lonsdale MN, Stroobants SG, et al. FDG PET and PET / CT : EANM procedure guidelines for tumour PET imaging : version 1 . 0. Eur J Nucl Med Mol Imaging. 2009;37(1):181–200.

3. Avril NE, Weber WA. Monitoring response to treatment in patients utilizing PET. Radiol Clin North Am. 2005;43:189–204.

4. Bastiaannet E, Groen H, Jager PL, Cobben DCP, Graaf WTA Van Der, Vaalburg W, et al. The value of FDG-PET in the detection , grading and response to therapy of soft tissue and bone sarcomas ; a systematic review and meta-analysis. Cancer Treat Rev. 2004;30:83–101.

5. Borst GR, Belderbos JSA, Boellaard R, Comans EFI, Jaeger K De, Lammertsma AA, et al. Standardised FDG uptake : A prognostic factor for inoperable non-small cell lung cancer. Eur J Cancer. 2005;41:1533–41.

6. Fletcher JW, Djulbegovic B, Soares HP, Siegel BA, Lowe VJ, Lyman GH, et al. Recommendations on the Use of PET in Oncology. J Nucl Med. 2008;49(3):480–509.

7. Kaalep A, Sera T, Oyen W, Krause BJ, Chiti A, Liu Y, et al. EANM/EARL FDG-PET/CT accreditation - summary results from the first 200 accredited imaging systems. Eur J Nucl Med Mol Imaging. 2018;45(3):412–22.

8. Wang W, Hu Z, Gualtieri EE, Parma MJ, Walsh ES, Sebok D, et al. Systematic and Distributed Time-of-Flight List Mode PET Reconstruction. 2006;

9. Surti S, Kuhn A, Werner ME, Perkins AE, Kolthammer J, Karp JS. Performance of Philips Gemini TF PET / CT Scanner with Special Consideration for Its Time-of-Flight Imaging Capabilities. J Nucl Med. 2007;48(3):471–81.

10. Surti S, Scheuermann J, Fakhri G El, Daube-witherspoon ME, Lim R, Abi-hatem N, et al. Impact of Time-of-Flight PET on Whole-Body Oncology Studies: A Human Observer Lesion Detection and Localization Study. J Nucl Med. 2011;52(5):712–20.

11. Miller MA. Focusing on high performance, Advanced Molecular Imaging, Vereos PET/CT. 2016.

12. Slomka PJ, Pan T, Germano G. Recent Advances and Future Progress in PET Instrumentation. Semin Nucl Med. 2016;46(1):5–19.

13. Vos CS Van Der, Koopman D, Rijnsdorp S, Arends AJ, Boellaard R, Dalen JA Van, et al. Quantification , improvement , and harmonization of small lesion detection with state-of-the-art PET. Eur J Nucl Med Mol Imaging [Internet]. 2017; Available from: http://dx.doi.org/10.1007/s00259-017-3727-z

14. Koopman D, Dalen JA Van, Lagerweij MCM, Arkies H, Boer J De, Oostdijk AHJ, et al. Improving the Detection of Small Lesions Using a State-of-the-Art Time-of-Flight PET/CT System and Small-Voxel Reconstructions. J Nucl Med Technol. 2015;43(1):21–7.

15. Koopman D, Koerkamp MG, Jager PL, Arkies H, Knollema S, Slump CH, et al. Digital PET compliance to EARL accreditation specifications. Springer Nat. 2017;

16. Kelloff GJ, Hoffman JM, Johnson B, Scher HI, Siegel B, Cheng EY, et al. Progress and Promise of FDG-PET Imaging for Cancer Patient Management and Oncologic Drug Development. Am Assoc Cancer Res. 2005;11(8):2785–809.

17. Shankar LK, Hoffman JM, Bacharach S, Graham MM, Karp J, Lammertsma AA, et al. Consensus Recommendations for the Use of 18 F- FDG PET as an Indicator of Therapeutic Response in Patients in National Cancer Institute Trials. J Nucl Med. 2006;47(6):1059–67.

18. Beadsmoore C, Newman D, MacIver D, Pawaroo D. Positron emission tomography computed tomography: A guide for the general radiologist. Can Assoc Radiol J [Internet]. 2015;66(4):332–47. Available from: http://dx.doi.org/10.1016/j.carj.2015.02.003

19. Badawi R. Introduction to PET Physics [Internet]. 1999. Available from: https://depts.washington.edu/nucmed/IRL/pet_intro/toc.html

20. Boellaard R, Delgado-bolton R, Oyen WJG, Giammarile F, Tatsch K, Eschner W, et al. FDG PET / CT : EANM procedure guidelines for tumour imaging : version 2 . 0. Eur J Nucl Med Mol Imaging. 2015;42(1):328–54.

21. Boellaard R, Willemsen A, Arends B, Visser EP. EARL procedure for assessing PET/CT system specific patient FDG activity preparations for quantitative FDG PET/CT studies. April 2013 [Internet]. 2010;1–3. Available from: http://earl.eanm.org/html/img/pool/EARL-procedure-for-optimizing-FDG-activity-for-quantitative-FDG-PET-studies_version_1_1.pdf

22. Koopman D, Osch JAC Van, Jager PL, Tenbergen CJA, Knollema S, Slump CH, et al. Technical note : how to determine the FDG activity for tumour PET imaging that satisfies European guidelines. EJNMMI Phys [Internet]. 2016; Available from: http://dx.doi.org/10.1186/s40658-016-0158-z

23. EARL, FDG-PET/CT Accreditation [Internet]. European Association of Nuclear Medicine. 2018 [cited 2018 Apr 15]. Available from: http://earl.eanm.org/cms/website.php

24. Halpern BS, Dahlbom M, Quon A, Schiepers C, Waldherr C, Silverman DH, et al. Impact of Patient Weight and Emission Scan Duration on PET/CT Image Quality and Lesion Detectability. J Nucl Med. 2004;45:797–801.

25. Halpern BS, Dahlbom M, Auerbach M a, Schiepers C, Fueger BJ, Weber W a, et al. Optimizing imaging protocols for overweight and obese patients: a lutetium orthosilicate PET/CT study. J Nucl Med. 2005;46:603–7.

26. Everaert H, Vanhove C, Lahoutte T, Muylle K, Caveliers V, Bossuyt A, et al. Optimal dose of 18F-FDG required for whole-body PET using an LSO PET camera. Eur J Nucl Med Mol Imaging. 2003;30(12):1615–9.

27. Watson CC, Casey ME, Bendriem B, Carney JP, Townsend DW, Eberl S, et al. Optimizing injected dose in clinical PET by accurately modeling the counting-rate response functions specific to individual patient scans. J Nucl Med [Internet]. 2005;46(11):1825–34. Available from: http://www.ncbi.nlm.nih.gov/pubmed/16269596

28. Masuda Y, Kondo C, Matsuo Y, Uetani M, Kusakabe K. Comparison of Imaging

Protocols for 18F-FDG PET/CT in Overweight Patients: Optimizing Scan Duration Versus Administered Dose. J Nucl Med [Internet]. 2009;50(6):844–8. Available from: http://jnm.snmjournals.org/cgi/doi/10.2967/jnumed.108.060590

29. de Groot EH, Post N, Boellaard R, Wagenaar NRL, Willemsen ATM, van Dalen JA. Optimized dose regimen for whole-body FDG-PET imaging. EJNMMI Res. 2013;3(1):1–11.

30. Date V, Number V, Investigator P, Walsh C, Title P, Device SUA, et al. Research Protocol PETPET study. 2.0. Zwolle; 2018. 1-26 p.

31. Koopman D. Digitale PET: het recept voor lage dosering en snel scannen? 2018; Available from: https://mtintegraal.nl/artikelen/657/digitale-pet-het-recept-voor-lage-dosering-en-snel-scannen

32. Surti S. Update on Time-of-Flight PET Imaging. J Nucl Med [Internet]. 2015;56(1):98–105. Available from: http://jnm.snmjournals.org/cgi/doi/10.2967/jnumed.114.145029

33. Chang T, Chang G, Clark JW, Diab RH, Rohren E, Mawlawi OR. Reliability of predicting image signal-to-noise ratio using noise equivalent count rate in PET imaging. Med Phys. 2012;39(10):5891–900.

34. van Sluis JJ, de Jong J, Schaar J, Noordzij W, van Snick P, Dierckx R, et al. Performance characteristics of the digital Biograph Vision PET/CT system. J Nucl Med [Internet]. 2019;jnumed.118.215418. Available from: http://jnm.snmjournals.org/lookup/doi/10.2967/jnumed.118.215418

35. Zhang J, Maniawski P, Knopp M V. Performance evaluation of the next generation solid-state digital photon counting PET / CT system. 2018;

36. Gambhir SS, Czernin J, Schwimmer J, Silverman DHS, Coleman RE, Phelps ME. A Tabulated Summary of the FDG PET Literature. J Nucl Med [Internet]. 2001;42:1S–93S. Available from: http://www.ncbi.nlm.nih.gov/pubmed/11884507%5Cnhttp://jnm.snmjournals.org/content/43/3/441.long%5Cnhttp://jnm.snmjournals.org/content/43/3/441.full.pdf+html

37. Takamochi K, Yoshida J, Murakami K, Niho S, Ishii G, Nishimura M, et al. Pitfalls in lymph node staging with positron emission tomography in non-small cell lung cancer patients. Lung Cancer. 2005;47(2):235–42.

38. Soret M, Bacharach SL, Buvat I. Partial-Volume Effect in PET Tumor Imaging*. J Nucl Med. 2007;48(6):932–46.

39. Koopman D, Dalen JA Van, Arkies H, Oostdijk AHJ, Francken AB, Bart J, et al. Diagnostic implications of a small-voxel reconstruction for loco-regional lymph node characterization in breast cancer patients using FDG-PET / CT. Springer Nat. 2018;

40. Adler S, Seidel J, Choyke P, Knopp M V., Binzel K, Zhang J, et al. Minimum lesion detectability as a measure of PET system performance. EJNMMI Phys. 2017;4(1).

41. Moses W. Fundamental Limits of Spatial Resolution in PET. Nucl Instrum Methods. 2011;165(9):1093–5.

42. Kaalep A, Sera T, Rijnsdorp S, Yaqub M, Talsma A, Lodge MA, et al. Feasibility of state of the art PET/CT systems performance harmonisation. Eur J Nucl Med Mol Imaging. 2018;45(8):1344–61.

Appendix

A. Additional information Chapter II 2
A.1. Choices reconstruction settings 2
A.2. Results with original EARL reconstruction settings 6
A.3. Results based on adjusted effective sensitivities 10
B. Additional information Chapter III 12
B.1. Compliance to EARL 2.0 12

A. Additional information Chapter II

A.1. Choices reconstruction settings

At the start of the study we only had acquired data from the Philips Ingenuity, Philips Vereos, and the GE Discovery D690 PET/CT systems. We did not test the effect of adjusting the reconstruction settings of the two Philips scanners. We did investigate the effect of adjusting the Gaussian smoothing filter to 5 mm for the Discovery D690, because we found the recommended 6.4 mm filter quite specific. In order to determine which reconstruction resulted in RC curves with the least variation from the RC curves of the other two PET systems, we calculated the absolute deviation (D) of the RC_{max} per sphere of the average RC_{max} of the other two PET systems with the following equation:

$$D = \frac{RC_{max,s} - RC_{max,i}}{RC_{max,i}} \cdot 100\%$$

$RC_{max,s}$ represents the RCmax of one of the spheres on the Discovery D690 scan and $RC_{max,i}$ represents the average RCmax of the sphere of the other 2 PET systems. The absolute deviation of the RC_{mean} was determined in a similar way. The results are shown in Table A.1. The reconstruction which, on average, deviated least from the other two PET systems, was chosen to be used in the study.

Table A.1: The deviation of the RC_{max} of the GE Discovery D690 from the average RC_{max} of the Philips Ingenuity and the Philips Vereos (A) and the deviation of the RC_{mean} of the GE Discovery D690 from the average RC_{mean} of the two Philips systems (B). The reconstruction which, on average, deviated least from the other two PET scanners, is indicated by a red box.

		Deviation			
Diameter (mm)	Average RCmax	Ingenuity	Vereos	Discovery D690 G=6.4mm	Discovery D690 G=5mm
37	1.00	0.0%	0.0%	0.0%	0.0%
28	1.00	0.8%	0.8%	3.9%	3.3%
22	0.99	1.7%	1.7%	2.3%	2.9%
17	0.93	0.6%	0.6%	2.5%	2.0%
13	0.75	3.7%	3.7%	2.1%	4.3%
10	0.45	8.2%	8.2%	5.0%	16.9%
	Average	2.5%	2.5%	2.7%	4.9%

A

		Deviation			
Diameter (mm)	Average Rcmean	Ingenuity	Vereos	Discovery D690 G=6.4mm	Discovery D690 G=5mm
37	0.81	1.9%	1.9%	1.2%	1.9%
28	0.78	1.1%	1.1%	1.4%	1.1%
22	0.70	3.8%	3.8%	4.9%	4.4%
17	0.64	4.4%	4.4%	4.1%	8.7%
13	0.49	3.8%	3.8%	7.4%	21.6%
10	0.33	1.7%	1.7%	10.2%	23.5%
	Average	2.8%	2.8%	4.9%	10.2%

B

When we included the Siemens Biograph mCT in the study, we determined the deviation of the RC_{max} and RC_{mean} curves from the other three PET systems in the same way. The results are shown in Table A.2. The reconstruction which, on average, deviated least from the other three PET systems, was chosen to be used in the study.

Table A.2: The deviation of the RC_{max} of the Siemens Biograph mCT from the average RC_{max} of the Philips Ingenuity, Philips Vereos, and GE Discovery D690 (A) and the deviation of the RC_{mean} from the average RC_{mean} of the other three systems (B). The reconstruction which, on average, deviated least from the other two PET scanners, is indicated by a red box.

		Deviation				
Diameter (mm)	Average RCmax	Ingenuity	Vereos	Discovery D690 G=6.4mm	Biograph mCT G=7mm	Biograph mCT G=7.5mm
37	1.00	0.0%	0.0%	0.0%	0.3%	0.2%
28	0.98	3.3%	1.6%	1.6%	4.6%	0.4%
22	0.97	3.8%	0.3%	0.3%	4.2%	1.2%
17	0.92	2.1%	0.8%	1.1%	1.3%	2.1%
13	0.77	5.9%	1.4%	4.3%	16.0%	13.0%
10	0.50	16.9%	2.0%	4.9%	13.5%	12.1%
	Average	5.3%	1.0%	2.0%	6.6%	4.8%

A

		Deviation				
Diameter (mm)	Average Rcmean	Ingenuity	Vereos	Discovery D690 G=6.4mm	Biograph mCT G=7mm	Biograph mCT G=7.5mm
37	0.80	1.5%	2.3%	0.8%	1.6%	1.4%
28	0.77	0.6%	1.6%	0.9%	0.5%	0.9%
22	0.71	5.3%	2.1%	3.2%	2.4%	1.0%
17	0.65	5.7%	3.0%	2.7%	2.0%	2.0%
13	0.50	1.3%	6.1%	4.8%	2.8%	2.3%
10	0.35	4.9%	1.7%	6.6%	12.4%	10.5%
	Average	3.2%	2.8%	3.2%	3.6%	3.0%

B

In addition, we have been able to include the Siemens Biograph Vision. However, only one scan of this PET system was made available to us, so we did not test and compare different reconstruction settings.

Finally, the GE Discovery MI was included. With this PET system, we have been able to perform phantom scans ourselves and test various reconstruction settings. The comparison between the deviation of the initial reconstruction settings and the adjusted reconstruction settings are shown in Table A.3. The reconstruction which, on average, deviated least from the other five PET systems, was chosen to be used in the study.

Table A.3: The deviation of the RC_{max} of the GE Discovery MI from the average RC_{max} of the Philips Ingenuity, Philips Vereos, GE Discovery D690, Siemens Biograph mCT, and Siemens Biograph Vision (A) and the deviation of the RC_{mean} from the average RC_{mean} of the other five systems (B). The reconstruction which, on average, deviated least from the other two PET scanners, is indicated by a red box.

		Deviation						
Diameter (mm)	Average RCmax	Ingenuity	Vereos	Discovery D690 G=6.4mm	Biograph mCT G=7.5mm	Biograph Vision	Discovery MI 192x192 matrix	Discovery MI 128x128 matrix
37	1.00	0.0%	0.1%	0.0%	0.2%	0.0%	0.0%	0.1%
28	0.99	2.1%	0.5%	2.7%	0.7%	0.8%	1.7%	1.9%
22	0.98	2.7%	0.8%	1.4%	0.1%	0.5%	2.9%	4.2%
17	0.92	1.9%	0.7%	1.2%	2.3%	0.9%	3.4%	3.9%
13	0.73	0.9%	6.8%	0.8%	8.3%	1.5%	3.0%	4.5%
10	0.47	11.3%	4.5%	1.5%	6.2%	11.4%	15.3%	1.0%
	Average	3.1%	2.2%	1.3%	3.0%	2.5%	4.4%	2.6%

A

		Deviation						
Diameter (mm)	Average Rcmean	Ingenuity	Vereos	Discovery D690 G=6.4mm	Biograph mCT G=7.5mm	Biograph Vision	Discovery MI 192x192 matrix	Discovery MI 128x128 matrix
37	0.81	2.4%	1.3%	1.7%	2.4%	2.9%	3.0%	2.0%
28	0.78	0.9%	1.4%	1.2%	1.1%	0.7%	0.3%	0.4%
22	0.72	6.5%	0.8%	1.9%	2.2%	3.7%	2.7%	1.6%
17	0.66	6.3%	2.4%	2.1%	2.6%	1.9%	2.8%	0.6%
13	0.50	0.5%	6.8%	4.0%	3.1%	2.3%	4.6%	1.1%
10	0.35	6.4%	3.2%	4.9%	12.0%	4.8%	4.6%	1.8%
	Average	3.8%	2.7%	2.6%	3.9%	2.7%	3.0%	1.3%

B

A.2. Results with original EARL reconstruction settings

The RC curves of all 6 PET systems, when the original EARL reconstruction settings were used, are shown in Figure A.1. In Figure A.2, the power-law fits of the COVs in de background compartment are presented as a function of the scan duration. The values of the power-law fit parameters (a and b), the resulting minimal scan times (Tmin), and System Constants (C_{sys}) are shown in Table A.4.

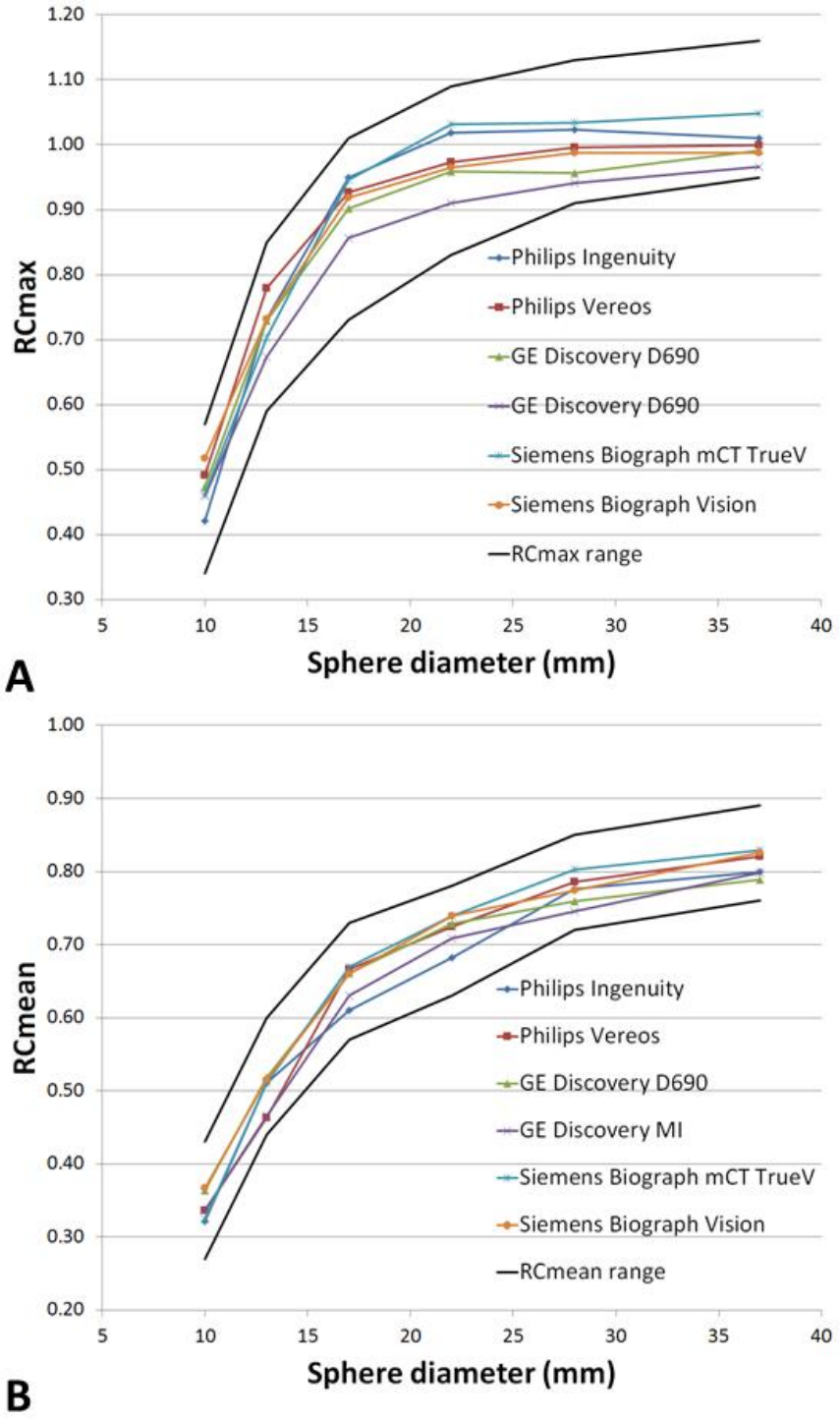

Figure A.1: RCmax (A) and RCmean curves for all six PET scanners, using the original EARL reconstruction settings. All RC's were within EARL specifications.

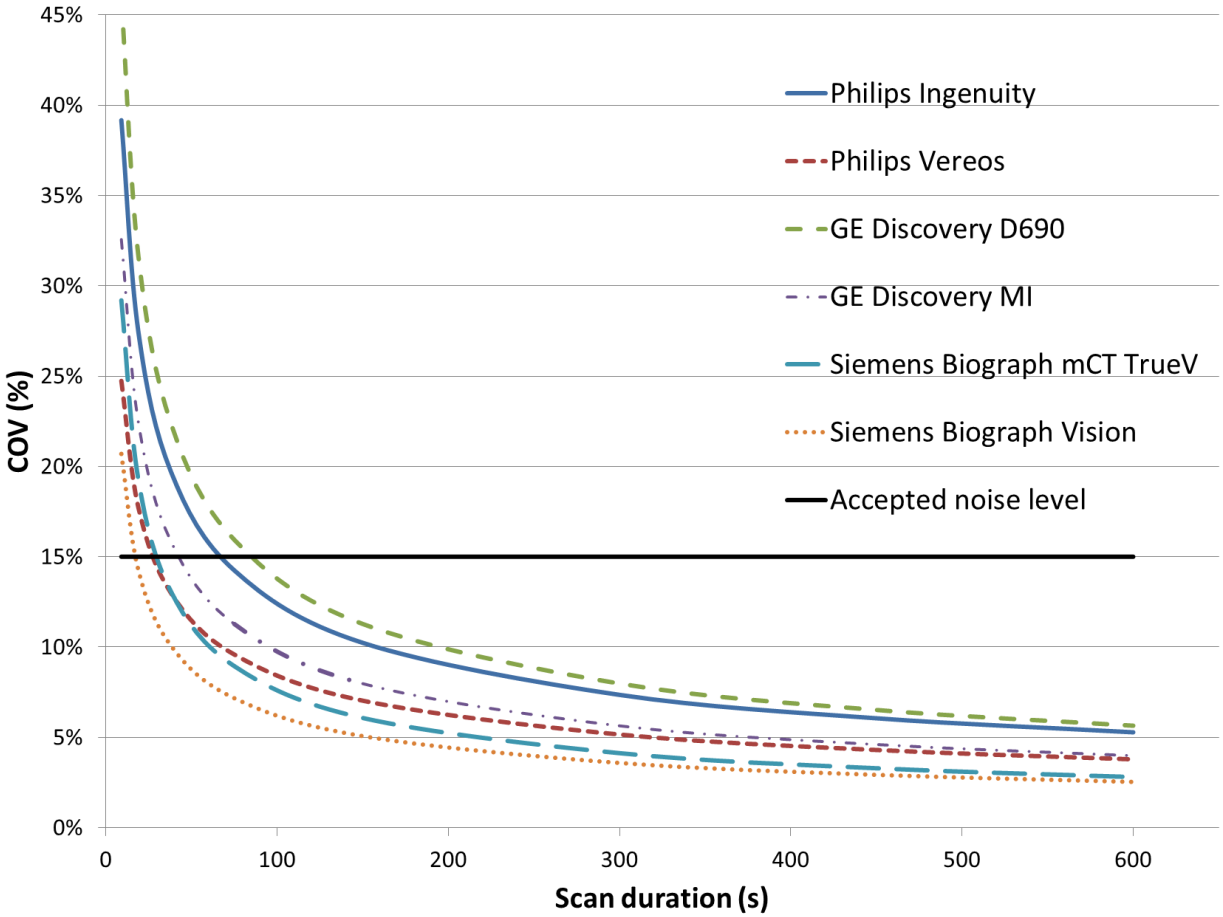

Figure A.2: C_{sys} of each PET system, based on the original EARL reconstruction settings plotted against their effective sensitivity (S_e). A power-law fit is included (R2 = 0.79).

Table A.4: The power-law fits resulted in the parameters a and b with a coefficient of determination (R2), which indicates how well the trend line fits the data. Using COVmax, the resulting Tmin per PET system is displayed. For both the Discovery MI and the Biograph Vision shorter scan durations were not available for the original EARL reconstructions settings. Therefore R^2 could not be determined for their power-law fits.

		a	b	R²	Tmin (s)	System Constant
Philips	Ingenuity TF	1.117	0.477	0.995	61	3.27
	Vereos	0.660	0.447	0.990	40	2.12
GE	Discovery D690	1.374	0.499	0.997	60	3.18
	Discovery MI	0.977	0.500	-	45	1.75
Siemens	Biograph mCT TrueV	0.995	0.558	0.981	44	2.02
	Biograph Vision	0.621	0.500	-	26	1.36

The C_{sys} of each PET system is plotted against its S_e in Figure A.3. C_{sys} decreases with increasing S_e. A power-law fit describes the relation between C_{sys} and S_e with a $R^2 = 0.71$ and the following formula:

$$C_{sys} = 9.53 \cdot S_e^{-0.45}$$

This leads to the following body-weight (w) dependent formula for the product of FDG activity to administer (A) and scan time per bed position (t), applicable to any given PET/CT system:

$$A \cdot t = 9.53 \cdot S_e^{-0.45} \cdot w^2$$

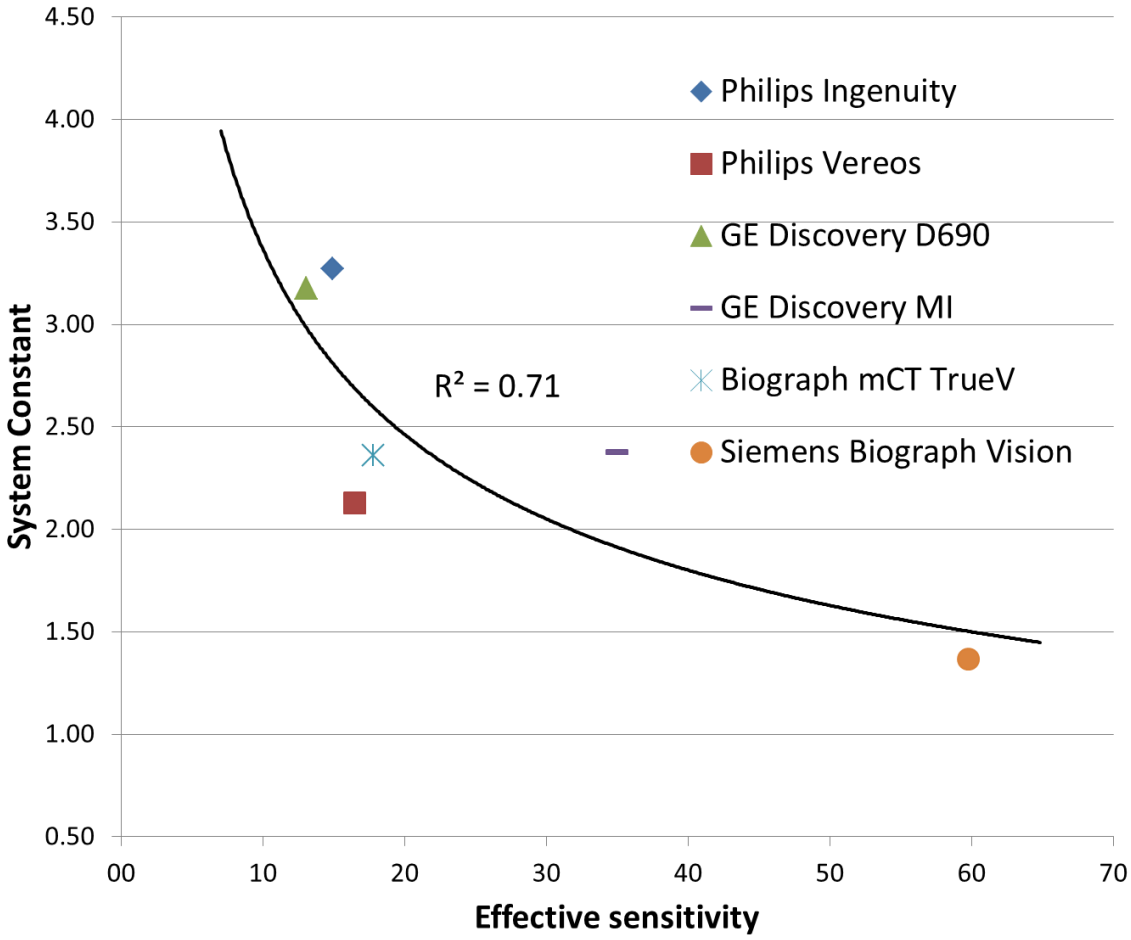

Figure A.3: C_{sys} of each PET system plotted against their S_E. A power-law fit is included ($R^2 = 0.71$).

A.3. Results based on adjusted effective sensitivities

The NEMA specifications of the Siemens Biograph Vision as determined by Sluis et al. (1) and the NEMA specifications of the other five PET systems as described by Zhang et al. (2) are shown in Table A.5.

Table A.5: The NEMA specifications per PET system (1,2). S_e is derived from the intrinsic sensitivity at center (S_i) and the timing resolution (Δt) by $S_i/\Delta t$.

Manufacturer	**Philips**		**GE**		**Siemens**	
PET/CT system	Ingenuity TF	Vereos	Discovery D690	Discovery MI	Biograph mCT TrueV	Biograph Vision
Photodetector	PMT	SiPM	PMT	SiPM	PMT	SiPM
S_i at center (kcps/MBq)	6.6	5.7	7.4	13.7	9.6	16.4
Δt (ps)	585	322	544	375	555	210
S_e (cps/MBq/ps)	11.3	17.7	13.6	36.5	17.3	78.1

The C_{sys} of each PET system (with the results of Chapter II by using adjusted reconstruction settings) plotted against the S_e (according to Table A.5) is shown in Figure A.4.

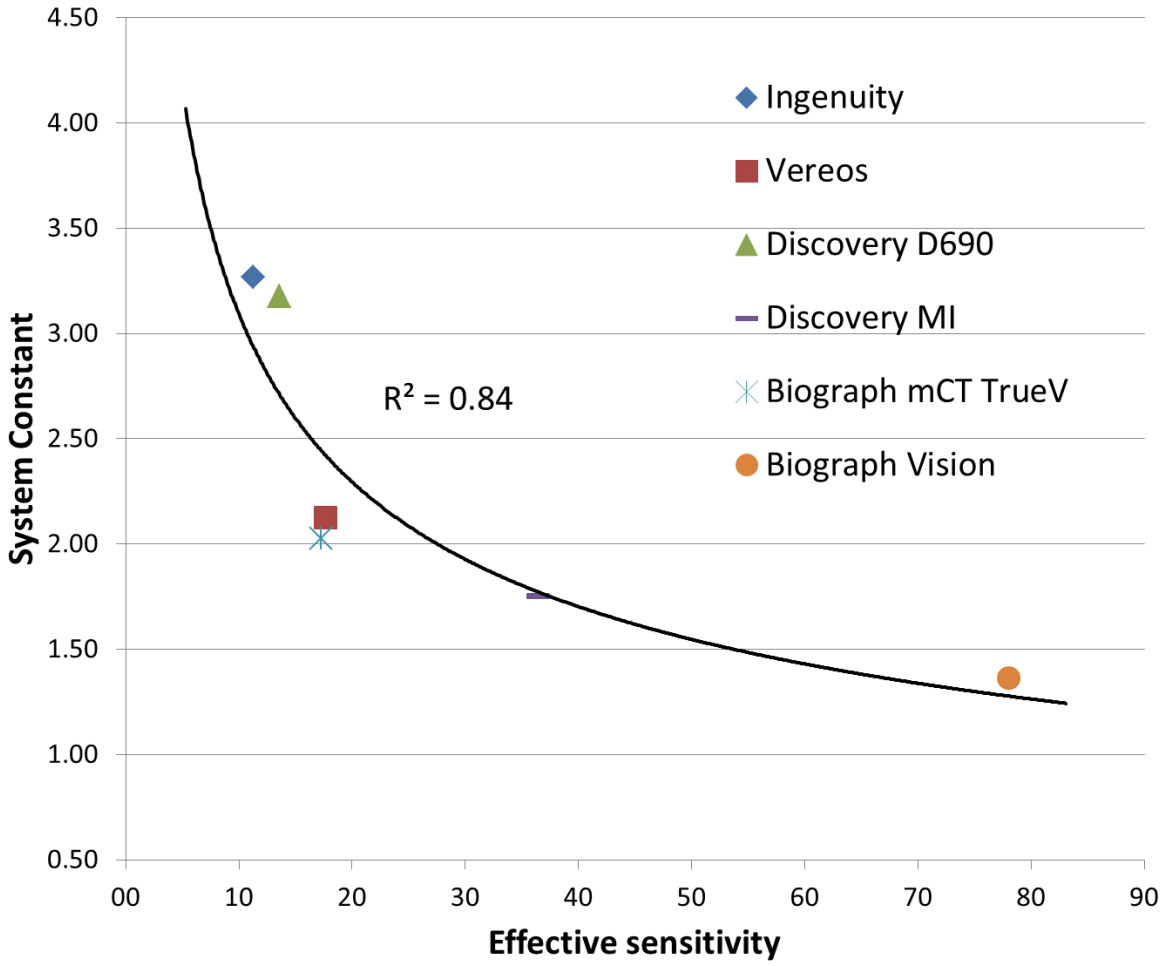

Figure A.4: C_{sys} of each PET system (according to results described in Chapter II) plotted against their S_e (1,2). A power-law fit is included ($R^2 = 0.84$).

The C_{sys} decreases with increasing S_e. A power-law fit describes the relation between C_{sys} and S_e with a $R^2 = 0.84$ and the following formula:

$$C_{sys} = 8.33 \cdot S_e^{-0.43}$$

This leads to the following body-weight (w) dependent formula for the product of FDG activity to administer (A) and scan time per bed position (t), applicable to any given PET/CT system:

$$A \cdot t = 8.33 \cdot S_e^{-0.43} \cdot w^2$$

B. Additional information Chapter III

B.1. Compliance to EARL 2.0

In recent years, new PET/CT systems have been developed with especially the digital photomultiplier technology being of great importance, and therefore the accreditation specifications that were described in the background section of Chapter I are becoming outdated. During the EANM Conference 2018 in Düsseldorf, EARL has announced an update of the current EARL performance specifications (3), which are shown in table 1. The updated specifications will become effective per January 2019 and a transition phase of two years is foreseen.

Table 1: The updated recovery coefficient (RC) specifications for VOI-MAX and VOI-A50 for all six spheres of the NEMA NU2-2001 IQ phantom that will become effective per January 2019 (3).

		VOI-MAX		VOI-A50	
Sphere Diameter (mm)	Sphere Volume (mL)	Minimal RC	Maximal RC	Minimal RC	Maximal RC
37	26.52	1.05	1.29	0.85	1.00
28	11.49	1.01	1.26	0.82	0.97
22	5.57	1.01	1.32	0.80	0.99
17	2.57	1.00	1.38	0.76	0.97
13	1.15	0.85	1.22	0.63	0.86
10	0.52	0.52	0.88	0.39	0.61

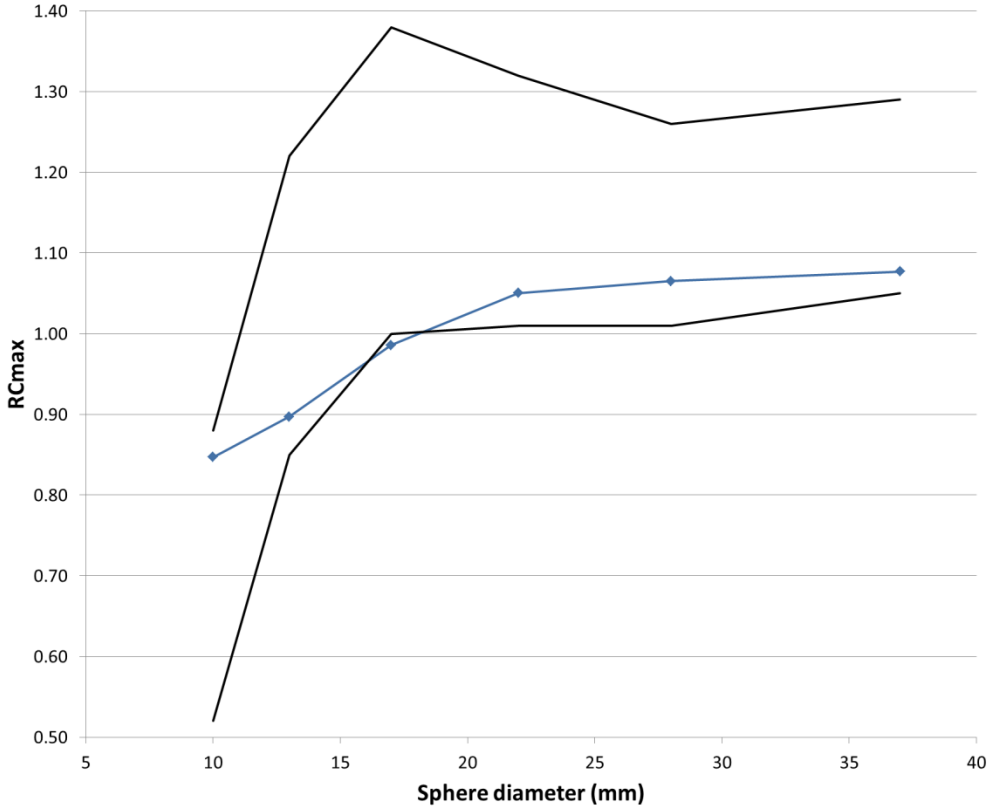

Figure 7: The 2x2x2 voxel reconstruction we used in the comparison with the uHR reconstruction in Chapter 3 is not completely in compliance with the updated EARL accreditation specifications for the RC_{max}.

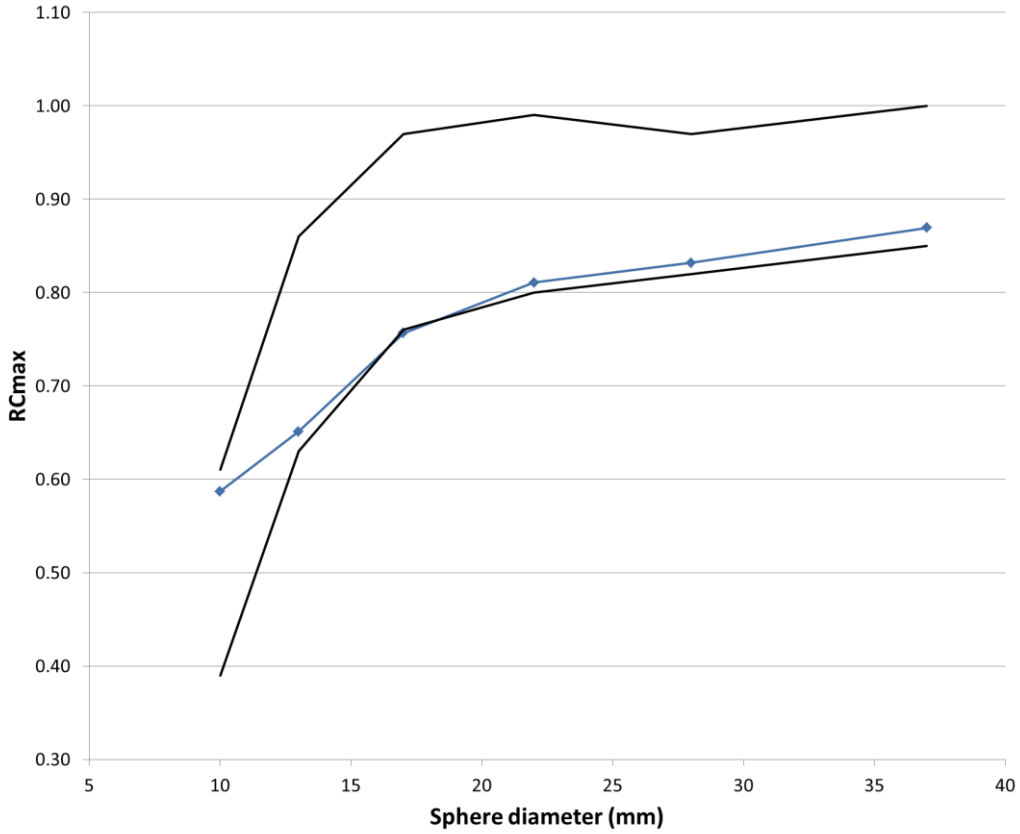

Figure 8: The 2x2x2 voxel reconstruction we used in the comparison with the uHR reconstruction in Chapter 3 is not completely in compliance with the updated EARL accreditation specifications for the RC_{mean}.